Petroleum Science 23 (2026) 4735–4752

Contents lists available at ScienceDirect

Petroleum Science

journal homepage: www.keaipublishing.com/en/journals/petroleum-science

Original Paper

Diagnostic potential of light hydrocarbons in deep marine natural gas: Insights from Tarim Basin

Zhi Chai [a,b], Zhong-Hong Chen [a,*], Moïse Luemba [a,c], Yong Chen [a], Fu-Lai Li [a]

[a] School of Geoscience, China University of Petroleum, Qingdao, 266580, Shandong, China
[b] School of Earth Sciences and Engineering, Xi'an Shiyou University, Xi'an, 710065, Shaanxi, China
[c] College of Resources and Environment, Yangtze University, Wuhan, 430100, Hubei, China

ARTICLE INFO

Article history:
Received 21 May 2025
Received in revised form
13 November 2025
Accepted 11 January 2026
Available online 16 January 2026

Edited by Min Li

Keywords:
Light hydrocarbons
Deep natural gas
Thermal cracking
Thermal maturity
Tarim Craton

ABSTRACT

Light hydrocarbons (LHs) retain comprehensive information about the genesis of natural gas. In this study, the gas composition, carbon isotopes, and LHs in deep marine natural gases from the Tarim Basin were comprehensively analyzed, along with comparative data on oil-cracked dry gases in the Sichuan Basin, to evaluate the diagnostic potential of LHs for deep natural gas genesis. The results demonstrate that the deep natural gases in the Tarim Craton are predominantly of thermogenic origin, sourced from sapropelic organic matter within marine shales. The analyzed gases exhibit maturities ranging from mature to over-mature stages, generated through both primary kerogen cracking and secondary cracking of oil and wet gas. These deep natural gases display distinct LH signatures at different thermal cracking stages. Initial cracking leads to an enrichment of *n*-alkanes, while the severe cracking stage (wet gas cracking stage) results in a pronounced shift toward *cyclo*-alkanes and aromatics. LH indicators related to the organic matter type and source rock lithology remain reliable during the initial cracking stage but become distorted under the severe cracking stage. The K_1 genetic comparison index and the 2,4-/2,3-dimethylpentane ratio retain diagnostic validity across all cracking stages, whereas other genetic comparisons and thermal maturity parameters are only applicable in the initial cracking stage. Additionally, ratios associated with biodegradation and evaporative fractionation are influenced by thermal cracking. Several ratios, such as methylcyclohexane/*n*-heptane, methylcyclohexane/cyclohexane, and (2- + 3-) methylhexane/*n*-hexane effectively differentiate primary cracking gases from severely cracked gases. The latter are characterized by elevated *cyclo*-alkane to *n*-alkane ratios of the C_6 range and aromatic to aliphatic ratios of the C_6–C_7 range, suggesting their potential as novel proxies for cracking intensity. Furthermore, similar to the 2,4-/2,3-dimethylpentane ratio, the two ratios of 2,2-/2,3- and 3,3-/2,3-dimethylpentane exhibit a systematic increase with thermal maturity, indicating their promise as robust indicators of thermal stress.

1. Introduction

Light hydrocarbons (LHs), originally defined in the context of crude oil, encompass C_5–C_{13} compounds with boiling points below 200 °C (Feng et al., 2022; Mango, 2000; Zhang et al., 2025). Subsequent research has extended this definition to natural gas, where LHs are more narrowly characterized as C_5–C_{10} compounds that remain liquid under standard temperature and pressure conditions (Hu et al., 2018; Huang et al., 2022b). Although typically present in trace amounts, LHs exhibit structural diversity, comprising *n*-alkane, *iso*-alkane, *cyclo*-alkane, and aromatic components (Huang et al., 2022b; Zhang et al., 2025). This structural complexity enables LHs to encode extensive geochemical information regarding organic matter input, depositional environment, thermal maturity, and secondary alteration processes such as biodegradation, evaporative fractionation, water washing, and thermochemical sulfate reduction (TSR) (Chai and Chen, 2023; Huang et al., 2022b; Walters et al., 2015; Yu et al., 2024; Zhang et al., 2025).

LHs also serve as intermediates in thermal cracking, with C_{14}^{+} acting as precursors and C_1–C_4 hydrocarbons as final products (Chai

* Corresponding author.
E-mail address: hongczh@163.com (Z.-H. Chen).
Peer review under the responsibility of China University of Petroleum (Beijing).

https://doi.org/10.1016/j.petsci.2026.01.012

et al., 2026; Hill et al., 2003; Huang et al., 2022a, 2023). Despite growing interest in LHs geochemistry, systematic studies of their evolution during thermal cracking remain limited. Through integrated thermal simulation experiments and natural sample analyses, Hu et al. (2005, 2018) and Zhang (2008) established several LH ratios, such as methylcyclohexane/*n*-heptane (MCH/nC_7), MCH/cyclohexane (MCH/CH), 2- + 3-methylhexane/*n*-hexane [(2- + 3-) MH/nC_6], and 2,3-dimethylpentane/MCH (2,3-DMP/MCH), to distinguish oil-cracking gas from kerogen-degradation gas. Al Darouich et al. (2006) characterized the cracking behaviour of C_6–C_{14} aromatics; Rakotoalimanana et al. (2016a, 2016b) investigated the formation mechanisms of alkylbenzenes [benzene (Bz), toluene (Tol), and C_4-Bz] and *cyclo*-alkanes [CH, MCH, and methylcyclopentane (MCP)]. Cheng et al. (2018) analyzed the $\delta^{13}C$ and δD evolution of Tol and MCH during the aromatization. He et al. (2022) evaluated the clay mineral catalysis effects on the generation of trans-1,2-dimethylcyclopentane (DMCP), nC_7, MCH, and Tol. Huang et al. (2022a, 2023) developed an improved LHs extraction protocol for gold tube pyrolysis experiments, examining LHs yield and compositional changes under thermal cracking, thermal cracking with evaporation, and thermal cracking with biodegradation. However, these studies exhibit three key limitations for deep natural gas applications: (1) a narrow focus on dominant compounds (e.g., nC_7, MCH and Tol), rather than comprehensive LH distributions; (2) uncertainties in extrapolating lab-based pyrolysis to geological conditions; and (3) predominant analysis of liquid products, leaving applicability to deep natural gas unverified.

The application of LHs in identifying natural gas genesis within the Tarim Craton is gradually being promoted. Hu et al. (2008) reported that deep natural gases from the platform area of the Tarim Basin are of sapropelic origin, as indicated by light $\delta^{13}C$ values of Bz (<−23‰), Tol (<−24‰), CH (<−24‰), and MCH (<−24‰). These gases are characterized by a predominance of nC_7 in the C_7 fraction, and abundant *n*- and *iso*-alkanes in the C_5–C_7 range. Yu et al. (2013) also noted that LHs from the Tarim Basin platform exhibit high *n*- and *iso*-alkane contents, along with lighter $\delta^{13}C$ values of Bz, Tol, CH, and MCH compared to foreland coal-type gases, confirming their sapropelic origin. Similar compositional features were observed by Chen et al. (2010) in deep gases from the Yingmaili and Halahatang areas of the Tabei Uplift, where nC_7 dominates the C_7 fraction and *n*- or *iso*-alkanes are prevalent in the C_5–C_7 range, supporting a sapropelic origin. Wu et al. (2014a, 2014b) also identified similar LH characteristics in deep Ordovician natural gas from the Halahatang and Lunnan areas of the Tabei Uplift, indicating its predominant nature as sapropelic-type gas. More recently, Ma et al. (2021) documented consistent LH parameters, K_1 (1.01–1.11) and K_2 (0.19–0.38), in Ordovician natural gas from the Shunbei area, indicating the same source; high heptane value (19.28%–32.91%) and *iso*-heptane value (1.01–3.25) indicate a mature to highly mature stage, while the MCH index below 35% (24.76%–32.90%) and the C_5–C_7 LHs dominated by *n*- and *iso*-alkanes confirm a sapropelic origin. Yu et al. (2024) emphasized complex deep natural gas origins in the Tazhong and Tabei Uplifts, including gases derived from sapropelic kerogen degradation and oil cracking in early stages; the C_{5-7} LHs in both regions exhibit a predominance of *n*- and *iso*-alkanes. Although these studies have increased confidence in using LHs to identify the origin of deep natural gas, they are primarily based on gases that are either uncracked or in the early stages of cracking. Consequently, significant uncertainty remains regarding the reliability and applicability of LH indicators under conditions of severe thermal cracking.

This study presents new geochemical data from 25 natural gas samples from the Tarim Craton, integrated with systematically compiled published data. A comprehensive analysis was conducted on the C_1–C_4 compositions, stable carbon isotopes, and LHs in deep marine natural gases from the Tarim Craton, comparing them with typical thermally cracked dry gases from the Sichuan Basin. The objective was assessing the diagnostic potential of LH fingerprints in deep natural gas genesis characterization and suggesting novel indices for thermal maturity and cracking intensity evaluation. This framework advances the understanding of LH systematics in deep petroleum systems and provides a practical tool for exploring deep to ultra-deep gas reservoirs.

2. Geological setting

The Tarim Basin (approximately 56×10^4 km^2) is the largest inland petroliferous basin in China (Fig. 1(a)). This superimposed basin, which originated in the Neoproterozoic and developed on ancient continental crust, has evolved through successive rift, passive margin, cratonic, and foreland stages (Jia and Wei, 2002). The first structural units of the Basin comprise six depressions and five uplifts, including the Kuche Depression, Manjiaer Depression, Awati Depression, Tanggubasi Depression, Southwest Depression, Southeast Depression, Tadong Uplift, Tabei Uplift, Shuntuoguole Low Uplift, Tazhong Uplift, and Bachu Uplift (F. Chen et al., 2018; Zhu et al., 2014a). Based on the distribution of Paleozoic strata, the basin can be divided into two principal structural domains (Tang et al., 2019; Zhu et al., 2014b): a foreland region and a more extensive cratonic region. The latter contains the Tabei, Tazhong, and Bachu Uplifts; the Awati and Manjiaer Depressions; and the Shuntuoguole Low Uplift (Fig. 1(b)).

The Tarim Craton preserves a complete sedimentary succession ranging from the Sinian to Quaternary periods (Fig. 1(c)), with an average thickness of 12,000–13,000 m (Chai et al., 2020, 2022; Qiao et al., 2024; Sun et al., 2025). The Cambrian–Ordovician succession is dominated by marine deposits, including organic-rich mudstones and platform carbonates. The carbonate sequence, comprising dolomites and limestones with well-developed pore-cavity-fracture systems, forming the primary hydrocarbon-producing reservoirs in the region. These reservoir units are effectively sealed by laterally continuous mudstones, marls, tight chert beds, and evaporite deposits, which serve as excellent cap rocks (Chai et al., 2020, 2022; Sun et al., 2025; Zhu et al., 2021). The Silurian–Permian interval consists of transitional marine–terrestrial sequences, including clastic, carbonate, and igneous lithologies. The overlying Triassic–Quaternary section is represented by continental clastic deposits.

Numerous studies have confirmed that the Cambrian–Lower Ordovician (ϵ_1–O_1) and Middle–Upper Ordovician (O_{2-3}) successions constitute the principal marine source rocks (SRs) in the Tarim Craton (Cai et al., 2009, 2015; Z. Chen et al., 2018; Qiao et al., 2024; Sun et al., 2025; Zhang et al., 2012, 2022). The ϵ_1–O_1 SRs are primarily developed in the Xishanbulak ($\epsilon_1 x$), Xidashan ($\epsilon_1 xd$), Yuertusi ($\epsilon_1 y$), and Heituao ($O_{1-2}h$) formations. The $\epsilon_1 x$ and $\epsilon_1 xd$ SRs, encountered in wells such as TD1, TD2, and ML1 in the Tadong Uplift, consist of calcareous, siliceous mudstones, and marlstones. Their effective SR thickness (TOC $\geq$ 0.5%) exceeds 150 m, with TOC values ranging from 1.1% to 7.8% (Zhang et al., 2022). The $\epsilon_1 y$ SRs, documented in the Keping outcrop (northwestern Basin) and in wells including XH1, LT1, LT3, and QT1 in the Tabei Uplift, have an average thickness of 32.7 m (Yang et al., 2020; Zhang et al., 2012, 2022; Zhu et al., 2018, 2021). Deposition occurred during two transgressive cycles, each producing organic-rich mudstone and shale. The basal transgressive unit comprises phosphatic siliceous and mudstone interbedding with exceptionally high TOC (avg. 7.3%, up to 20.6%), whereas the upper cycle consists of dolomitic fine sandstone with lower TOC (0.4%–1.8%). The $O_{1-2}h$ SRs are present in the eastern Tarim Basin, with thicknesses ranging from

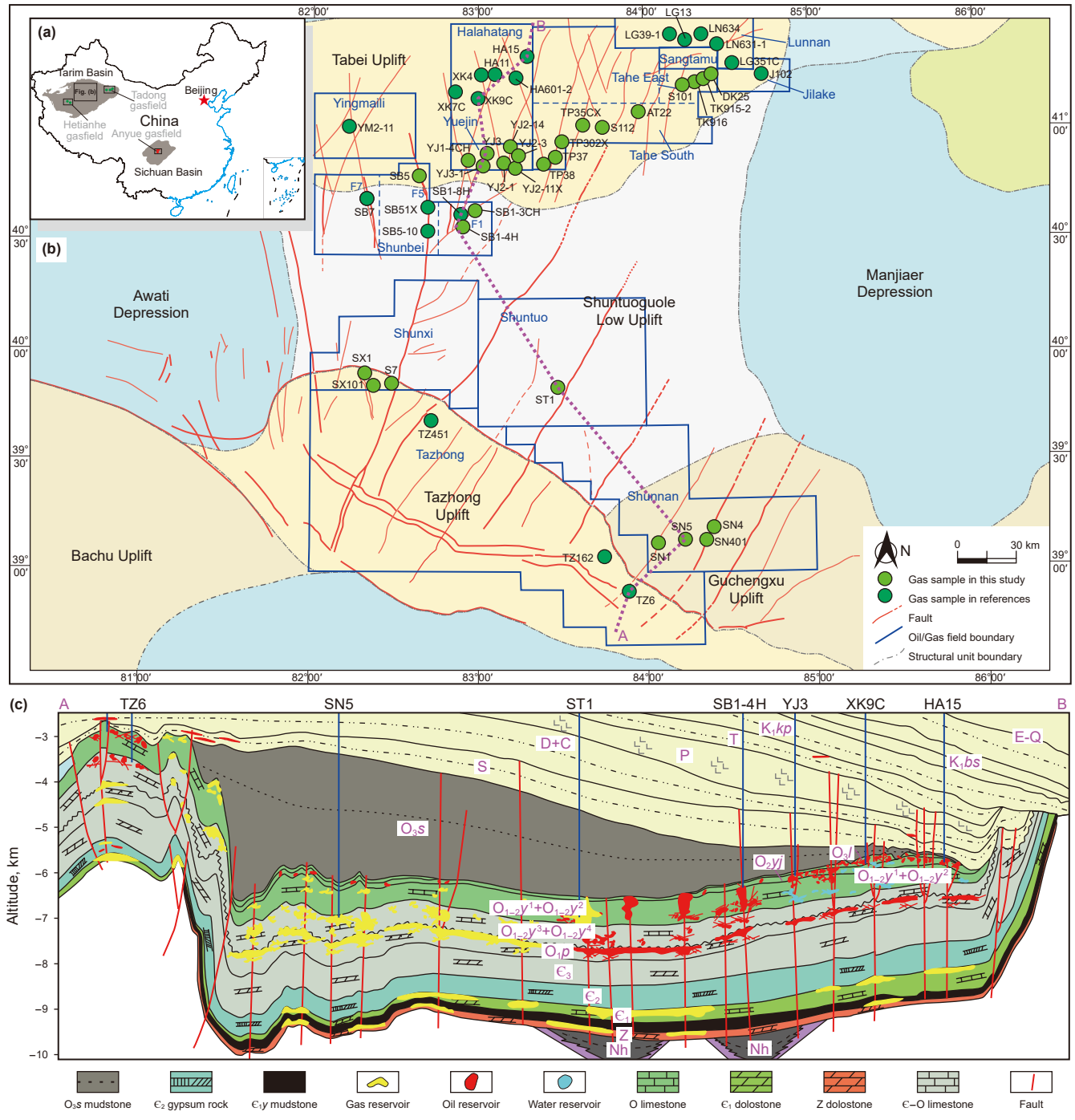

Fig. 1. Maps showing the location **(a)**, structural divisions and distribution of sampling wells **(b)**, and stratigraphic distribution **(c)** of the Tarim Craton. Nh, Nanhuan system; Z, Sinian; Є, Cambrian; O, Ordovician; O_1p, Penglaiba Formation; $O_{1\text{-}2}y$, Yingshan Formation; O_2yj, Yijinfang Formation; O_3l, Lianglitage Formation; O_3s, Sangtamu Formation; S, Silurian; D, Devonian; C, Carboniferous; P, Permian; T, Triassic; K, Cretaceous; K_1kp, Kapushaliang Formation; K_1bs, Bashijiqike Formation; E-Q, Paleogene-Quaternary.

48 m (TD1) to 190.5 m (ML1). TOC values exceed 1.0% in the YD2 and ML1 wells (reaching up to 5.8%) and range between 1.08% and 2.19% in the Querqueke outcrop in the eastern basin (Zhang et al., 2022). The $O_{2\text{–}3}$ SRs mainly include the Saergan ($O_{2\text{-}3}s$) and Yingan (O_3y) black shales in the Awati Depression and Keping outcrop (max. thickness ~30 m; TOC: 1.2%–5.6%), the Tumuxiuke ($O_{2\text{–}3}t$), Qiaerbake (O_3q) and Lianglitage (O_3l) mudstone, argillaceous limestone, and marlstone distributed on the slopes of the Tazhong and Tabei uplifts (max thickness ~100 m; avg. TOC: 0.84%) (Jin et al., 2017; He et al., 2025; Ma et al., 2020; Wang et al., 2024; Zhang et al., 2022).

3. Samples and methods

3.1. Samples

For this investigation, 25 deep natural gas samples were collected from Ordovician carbonate reservoirs across seven major oil and gas fields in the Tarim Craton: Tahe East, Tahe South, Yuejin, Shunbei, Shunxi, Shuntuo, and Shunnan (Fig. 1(b); Table 1). Due to the high volatility of natural gas, all samples were collected directly at the wellhead using highly sealed steel cylinders. Prior to sampling, each cylinder was evacuated to a high vacuum. The

Table 1
Composition and carbon isotopic ratios of deep marine natural gases in the Tarim Craton analyzed in this study.

Location	Well	Depth, m	Strata	Molar component contents, %					Molar component ratios					Carbon isotopes, ‰		
				C_1	C_2	C_3	C_4	C_{5+}	C_1/C_{1-5}	C_1/C_{2+3}	ln (C_1/C_2)	ln (C_2/C_3)	C_2/C_3	$\delta^{13}C_1$	$\delta^{13}C_2$	$\delta^{13}C_3$
Tahe-East (THE)	TK915-1	5748–5882	O_2	94.32	1.14	0.29	0.14	0.07	0.98	65.96	4.42	1.37	3.93	−32.28	−32	−29.55
	S101	5756–5817	O_2	95.3	1.4	0.39	0.25	0.12	0.98	53.24	4.22	1.28	3.59	−34.3	−33.3	−32.5
	TK916	5773–5839	O_2	92.78	1.25	0.41	0.27	0.13	0.98	55.89	4.31	1.11	3.05	−33.1	−33.3	−31.6
	DK25-1	5900–5968	O_2	92.11	1.82	0.51	0.23	0.11	0.97	39.53	3.92	1.27	3.57	−33.9	−37.9	−35.3
Tahe-South (THS)	TP35CX	6335–6363	O_{2-3}	60.11	11.65	5.48	1.92	0	0.76	3.51	1.64	0.75	2.13	−46.4	−37.6	−33.6
	TP37	6804–6940	O_2	73.6	11.85	4.41	1.36	0.3	0.8	4.53	1.83	0.99	2.69	−48.8	−37.1	−33.8
	TP302X	6209–6853	O_2	65.73	11.65	4.43	1.55	0	0.79	4.09	1.73	0.97	2.63	−46.98	−36.3	−33.8
	S112	6147–6200	O_2	76.4	8.36	5.03	3.12	1.29	0.81	5.71	2.21	0.51	1.66	−45.7	−36.9	−34.1
	TP38	6964–7071	O_2	74.58	11.56	4.15	1.23	0.27	0.81	4.75	1.86	1.02	2.79	−39.3	−31.8	−28.5
	AT22	6272–6404	O_2	88.25	4.84	2.22	0.74	0.2	0.92	12.5	2.9	0.78	2.18	−41.2	−36.6	−33
Yuejin (YJ)	YJ2-14	7083–7166	O_2	50.92	10.45	5.03	1.63	0.44	0.74	3.29	1.58	0.73	2.08	−42.5	−36.3	−33.1
	YJ1-4CH	7194–7773	O_2	76.38	7.5	4.33	3.21	1.37	0.82	6.46	2.32	0.55	1.73	−45.4	−34	−31.3
	YJ2-1	7109–7202	O_{2-3}	85.35	7.05	2.92	1.36	0.37	0.88	8.56	2.49	0.88	2.41	−46.1	−34.2	−31.6
	YJ3	7143–7208	O_2	84.86	6.69	2.86	1.25	0.27	0.88	8.89	2.54	0.85	2.34	n.d.	n.d.	n.d.
	YJ3-1	7194–7323	O_2	75.42	5.86	2.15	0.86	0.21	0.89	9.42	2.55	1.00	2.73	−34.5	−30.1	−29.1
	YJ2-11X	7343–7442	O_{1-2}	53.28	11.41	7.17	3.64	1.28	0.69	2.87	1.54	0.46	1.59	−52.7	−37.8	−33.8
Shunbei-F1 (SBF1)	SB1-3CH	7255–7357	O_2	83.73	6.99	3.25	1.75	0.51	0.87	8.18	2.48	0.77	2.15	−44.7	−33.3	−30.8
	SB1-4H	7459–7561	O_2	80.35	9.05	3.98	1.7	0.4	0.84	6.17	2.18	0.82	2.27	−47	−33.8	−31.6
Shunbei-F5 (SBF5)	SB5	7386–7387	O_2	54.48	17.97	9.43	3.24	0.82	0.63	1.99	1.11	0.65	1.91	−48.9	−39.3	−35.6
Shunxi (SX)	S7	6819–6912	O_{1-2}	84.91	3.12	1.2	1.18	1.28	0.93	19.66	3.3	0.95	2.6	−51.7	−32.5	−28.2
	SX1	6554–6583	O_3	85.56	5.62	2.2	1.25	0.43	0.9	10.94	2.72	0.94	2.55	−54.2	−36.5	−32.1
	SX101	6444–6600	O_3	82.07	6.89	3.34	1.66	0.47	0.87	8.02	2.48	0.72	2.06	n.d.	n.d.	n.d.
Shuntuo (ST)	ST1	7874	O_{1-2}	94.7	0.99	0.32	0.25	0.19	0.98	72.29	4.56	1.13	3.09	−39.2	−31.7	−29.5
Shunnan (SN)	SN4	6299–6688	O_{1-2}	88.86	0.47	0.09	0	0	0.99	160.11	5.24	1.71	5.53	−37.1	−31.5	−25.5
	SN5	7176–7209	O_1	96.74	0.08	0.003	0	0	1.00	1165.54	7.1	3.28	26.67	−35.9	−27.7	−20.8

Notes: n.d., not detected.

sampling procedure included purging the pipeline to eliminate residual air. Additionally, multiple cycles of pressurization and venting were employed to ensure complete displacement of dead volume within the cylinder. Following collection, samples were stored under cryogenic conditions and promptly transported to the laboratory for analysis.

To strengthen the dataset and enable comprehensive geochemical comparisons, an additional 150 published marine-sourced gas samples were incorporated from other major oil and gas fields in the Tarim and Sichuan basins. These include seven oil and gas fields in the Tarim Craton: Lunan, Jilake, Halahatang, Yingmaili, Tazhong, Tadong, and Hetianhe. Additionally, the dataset includes typical oil-cracking dry gases from the Sichuan Basin: Sinian–Cambrian (Z–€) gases within Anyue gas field, Carboniferous–Triassic (C–T) gases, and the Ordovician–Silurian (O–S) shale gases. All literature-derived data are documented in Supplementary Tables S1 and S2.

3.2. Gas analysis

Gas composition analysis was performed using an Agilent 6890 II gas chromatograph (GC) equipped with an HP-PLOT AL203 capillary column (50 m × 0.15 mm × 0.53 μm) and flame ionization detector. The temperature program began with an initial isothermal step at 32 °C for 5 min, followed by a linear temperature ramp at 15 °C/min to 180 °C, which was maintained for 10 min to ensure complete elution. Component quantification was achieved through external standard calibration.

Stable carbon isotope analysis of hydrocarbon gases was conducted using a Thermo Scientific Optima isotope ratio mass spectrometer interfaced with an HP 6890 II GC. The GC separation employed a temperature program starting at 40 °C with a ramp rate of 20 °C/h to 180 °C, followed by a 10 min isothermal period at 180 °C to ensure complete compound separation. All $\delta^{13}C$ values are reported relative to the Vienna Pee Dee Belemnite international standard.

To analyze LHs in dry gas, a concentration and enrichment procedure is essential. Specifically, natural gas is passed at low flow rates through a gas purification unit, followed by a light hydrocarbon enrichment column. This allows trace LHs to accumulate progressively within the enrichment system. Once an adequate amount has been concentrated, standard LHs analysis can be conducted. LH compositions were quantified using an Agilent 7890A GC system equipped with an HP-1 capillary column (60 m × 0.25 mm × 0.50 μm) and flame ionization detector. The temperature program was initiated with a 15 min isothermal hold at 35 °C, followed by a 2.5 °C/min ramp to 130 °C and a subsequent 20 °C/min ramp to 230 °C (with a final hold of 5 min). Compounds were identified through retention time matching against certified standards (Fig. 2), with abbreviations, full names, and key LH parameters provided in Tables 2 and 3.

4. Results

4.1. Gaseous components in deep natural gases

The natural gas samples from the Tarim Craton display a predominantly hydrocarbon-rich composition, with 86% of the samples containing more than 70% total hydrocarbons. Among these, methane (C_1) is the most abundant component, ranging from 28.00% to 98.23% (Fig. 3(a)), followed by progressively lower concentrations of ethane (C_2: 0.08%–20.92%), propane (C_3: 0–14.78%), butane (C_4: 0–9.44%), and pentanes plus (C_5^+: 0–7.40%).

The samples exhibit a wide variability in the dryness coefficient ($C_1/\Sigma C_{1-5}$), spanning from 0.52 to 1.00 (Fig. 3(a)). This range reflects a maturity continuum from wet to dry gas accumulations, indicative of genetic origins across the study area. Notably, gases from the Tahe East, Lunnan, Shunnan, Shuntuo, and Hetianhe areas

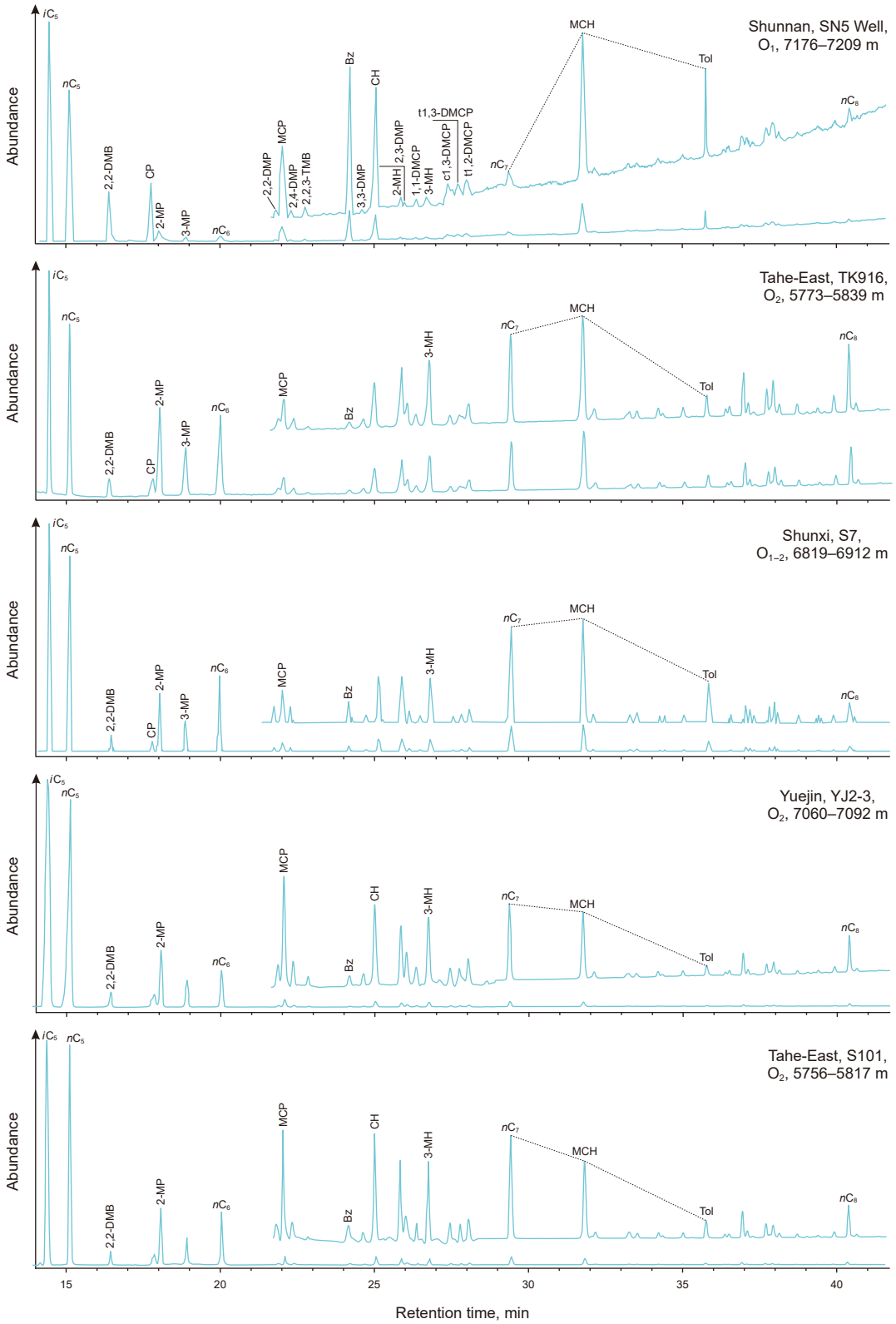

Fig. 2. Gas chromatograms showing the distribution of C_5–C_7 light hydrocarbons (LHs) in the deep natural gas from the Tarim Craton. See Table 2 for full names of LHs.

exhibit dry gas characteristics with dryness coefficient values approaching 1.0. These compositions show strong similarities to confirmed oil-cracking gases from the Anyue gas field in the Sichuan Basin (Zou et al., 2014; Hu et al., 2018). In contrast, gas samples from the Jilake, Tahe South, Shunxi, Shunbei, Yuejin, Halahatang, and Yingmaili areas exhibit wet gas signatures. Meanwhile, gas samples from the Tazhong and Tadong areas display transitional characteristics, predominantly of dry gases

Table 2
Abbreviations, full names, and calculation methods for some key parameters for light hydrocarbons (LHs).

No.	Abbreviations	LHs components	LHs parameters
1	iC_5	Isopentane	ΣDMCP = (1,1-DMCP + c1,3-DMCP + t1,3-DMCP + t1,2-DMCP)
2	nC_5	*n*-Pentane	$RCPC_7$ = ΣDMCP + 3-EP
3	2,2-DMB	2,2-Dimethylbutane	Thompson (1983):
4	CP	Cyclopentane	Heptane value (H) = (nC_7 × 100)/(CH + 2-MH + 2,3-DMP + 1,1-
5	2-MP	2-Methylpentane	DMCP + 3-MH + c1,3-DMCP + t1,3-DMCP + 3-EP + t1,2-
6	3-MP	3-Methylpentane	DMCP + nC_7 + MCH)
7	nC_6	*n*-Hexane	Isoheptane value (I) = (2 + 3)-MH/(c1,3 + t1,3 + t1,2)-DMCP
8	2,2-DMP	2,2-Dimethylpentane	Mango (2000):
9	MCP	Methylcyclopentane	$P_1 = nC_7$; P_2 = 2-MH + 3-MH
10	2,4-DMP	2,4-Dimethylpentane	P_3 = 3-EP + 3,3-DMP + 2,2-DMP + 2,3-DMP + 2,4-DMP + 2,2,3-TMB
11	2,2,3-TMB	2,2,3-Trimethylbutane	N_1^5 = ECP + t1,2-DMCP + c1,2DMCP
12	Bz	Benzene	N_1^6 = Tol + MCH
13	3,3-DMP	3,3-Dimethylpentane	N_2 = 1,1-DMCP + c1,3-DMCP + t1,3-DMCP
14	CH	Cyclohexane	K_1 = (2-MH + 2,3-DMP)/(3-MH + 2,4-DMP); $K_2 = P_3/(P_2 + N_2)$
15	2-MH	2-Methylhexane	Halpern (1995):
16	2,3-DMP	2,3-Dimethylpentane	C1 = 2,2-DMP/P_3; C2 = 2,3-DMP/P_3
17	1,1-DMCP	1,1-Dimethylcyclopentane	C3 = 2,4-DMP/P_3; C4 = 3,3-DMP/P_3
18	3-MH	3-Methylhexane	C5 = 3-EP/P_3
19	c1,3-DMCP	cis-1,3-Dimethylcyclopentane	TR1 = Tol/1,1-DMCP
20	t1,3-DMCP	trans-1,3-Dimethylcyclopentane	TR2 = nC_7/1,1-DMCP
21	3-EP	3-Ethylpentane	TR3 = 3-MH/1,1-DMCP
22	t1,2-DMCP	trans-1,2-Dimethylcyclopentane	TR4 = 2-MH/1,1-DMCP
23	nC_7	*n*-Heptane	TR5 = P_2/1,1-DMCP
24	MCH	Methylcyclohexane	TR6 = c1,2-DMCP/1,1-DMCP
25	ECP	Ethylcyclopentane	TR7 = t1,3-DMCP/1,1-DMCP;
26	Tol	Toluene	TR8 = P_2/P_3
27	nC_8	*n*-Octane	

(dryness coefficient >0.8 for most samples), with minor wet gas contributions.

4.2. Gaseous carbon isotopes in deep natural gases

The deep natural gases from the Tarim Craton display considerable variability in carbon isotopic composition. C_1 exhibits $\delta^{13}C$ values ranging from −54.40‰ to −32.28‰, while C_2 ranges from −41.40‰ to −26.20‰, and C_3 ranges from −51.60‰ to −20.80‰ (Fig. 3(b)). The carbon isotopic differences between components reveal $\delta^{13}C_1$–$\delta^{13}C_2$ values ranging from −19.2 ‰ to 4.0 ‰ and $\delta^{13}C_2$–$\delta^{13}C_3$ values of −6.9‰ to 21.3‰, indicating the presence of both normal and inverted carbon isotope sequences.

Statistical analysis shows that 87% of samples follow normal $\delta^{13}C$ sequences ($\delta^{13}C_1 < \delta^{13}C_2 < \delta^{13}C_3$). However, six samples from the Tazhong area exhibit a partial inversion sequence ($\delta^{13}C_1 < \delta^{13}C_2 > \delta^{13}C_3$), and ten samples from the Lunnan, Tahe East, Tadong, and Jilake areas display another partial inversion sequence ($\delta^{13}C_1 > \delta^{13}C_2 < \delta^{13}C_3$). These isotopic patterns are consistent with a thermogenic origin through Type II kerogen, although potential contributions from microbial oxidation or diffusion-mediated fractionation cannot be excluded (Liu et al., 2018, 2019; Zhou et al., 2019).

4.3. LHs in deep natural gases

LH compounds in the C_5–C_7 range were identified in the samples, with their compositional distributions presented in Fig. 2. Statistical analysis reveals significant variability in LH composition across the Tarim Craton samples. The relative abundances of *n*-alkanes (19.41%–56.84%), *iso*-alkanes (28.76%–66.77%), and *cyclo*-alkanes (1.71%–41.15%) exhibit no dominant compositional trend (Fig. 4(a)). Similarly, substantial variations occur in the proportions of *chain*-alkanes (*n*- and *iso*-alkanes), *cyclo*-alkanes, and aromatics. Within the C_6–C_7 range, *chain*-alkanes account for 19.21%–93.70%, *cyclo*-alkanes for 5.40%–49.27%, and aromatics for 0–31.52% (Fig. 4(b)). The C_7 distribution is further characterized by the relative abundances of *n*-heptane (nC_7), Σdimethylcyclopentane (ΣDMCP), and MCH (methylcyclohexane), which range from 6.53% to 73.00%, 5.40%–34.92%, and 20.81%–72.19%, respectively (Fig. 4(c)). Additionally, nC_7, MCH, and toluene (Tol) exhibit relative abundances of 5.24%–68.6%, 21.11%–60.61%, and 0%–36.76%, respectively.

Notably, the LHs distribution in certain samples, particularly gas from the Shunnan area SN5 well, shows striking similarities to oil-cracking dry gas from the Sichuan Basin. For instance, oil-cracking gas from the Sichuan Basin contains 5.5%–38% nC_7, 0%–40% ΣDMCP, and 40%–87.4% MCH, whereas a gas sample from the SN5 well contains 6.53% nC_7, 21.28% ΣDMCP, and 72.19% MCH (Fig. 4(c); Table 3). This comparison highlights a pronounced enrichment of MCH, suggesting that thermal cracking likely plays a key role in modifying LHs within these deep gases. This mechanism will be discussed in detail in the following section.

5. Discussion

5.1. Genesis of the gases

Establishing the origin and cracking degree of these deep natural gas samples forms a critical foundation for investigating LH's thermal cracking processes and associated parameters. Current methodologies for gas characterization rely heavily on analysis of gaseous components and isotopic compositions to determine origin, maturity, source, and secondary alteration (Milkov and Etiope, 2018; Milkov, 2021; Liu et al., 2018, 2019). The carbon isotopic signatures of the studied samples consistently plot within the sapropelic-sourced thermogenic domain on both the $\delta^{13}C_1$ versus $\delta^{13}C_2$ and $\delta^{13}C_2$–$\delta^{13}C_1$ versus $\delta^{13}C_1$ diagrams (Fig. 3(b) and (c)), indicating a predominantly sapropelic and thermogenic origin. This interpretation is further supported by the $\delta^{13}C_1$ versus $C_1/(C_2+C_3)$ diagram (Fig. 3(d)), in which samples cluster within the established field for oil-associated thermogenic gases. These diagnostic plots collectively indicate gas maturity ranging from mature to over-mature stages (Fig. 3). The SN5 well gas in the

Table 3
Light hydrocarbon ratios of deep marine natural gases in the Tarim Craton analyzed in this study.

Well	K_1	K_2	H	I	MCH/nC_7	RCPC$_7$/nC_7	MCH/CH	(2- + 3-) MH/nC_6
TK915-1	0.99	0.35	2.5	13.1	1.3	1.21	0.95	0.25
S101	1.08	0.38	2.94	20.2	0.82	0.69	0.9	0.28
TK916	1.04	0.37	3.27	17.42	1.45	0.8	2.33	0.86
DK25-1	0.95	0.39	2.58	13.82	1.38	1.08	0.9	0.27
TP35CX	1.02	0.39	1.97	19.81	0.72	0.75	0.7	0.19
TP37	1.01	0.26	1.54	18.14	1.16	0.81	0.9	0.23
TP302X	1.03	0.21	1.93	14.82	1.01	0.8	0.52	0.14
S112	1.09	0.18	2.03	18.51	0.83	0.76	0.69	0.22
TP38	n.d.	n.d.	n.d.	39.39	1.54	0	n.d.	n.d.
AT22	1.1	0.25	n.d.	24.17	0.7	0	0.58	0.21
YJ2-14	1.02	0.34	2.22	31.35	0.62	0.52	1.64	0.4
YJ1-4CH	1.05	0.37	2.69	21.57	0.69	0.74	0.9	0.2
YJ2-1	1.11	0.33	2.48	24.47	0.6	0.59	0.91	0.23
YJ2-3	0.99	0.32	2.39	16.15	0.98	0.99	0.81	0.21
YJ3	0.99	0.3	2.22	13.98	1.09	1.2	0.69	0.17
YJ3-1	1.06	0.33	2.4	28.24	0.55	0.47	1.04	0.26
YJ2-11X	1.1	0.33	2.3	22.76	0.56	0.64	0.63	0.2
SB1-3CH	1.09	0.31	3.01	26	0.52	0.46	0.81	0.2
SB1-4H	1.06	0.28	2.57	24.9	0.57	0.53	0.81	0.2
SB5	1.06	0.29	2.35	26.67	0.5	0.5	0.72	0.18
S7	1.12	0.44	4.29	23.88	0.8	0.44	1.24	0.33
SN4	1.09	0.49	2.62	23.81	0.77	0.58	1.21	0.37
SN5	0.95	0.57	0.59	3.89	11.06	3.26	1.19	0.69

Well	nC_{5-7}	iC_{5-7}	CyC$_{5-7}$	n + iC_{6-7}	CyC$_{6-7}$	AroC$_{6-7}$	nC_7	DMCP	MCH	nC_7	MCH	Tol
	%			%			%			%		
TK915-1	32.6	63.88	3.52	88.59	11.22	0.19	29.19	32.85	37.97	41.73	54.29	3.98
S101	39.94	52.85	7.21	82.44	16.01	1.55	41.03	25.23	33.74	50.71	41.71	7.58
TK916	30.28	49.52	20.2	71.39	26.3	2.31	31.9	21.71	46.39	37.58	54.65	7.77
DK25-1	39.61	51.98	8.41	81.52	17.13	1.35	29.66	29.36	40.98	39.06	53.97	6.97
TP35CX	38.88	56.72	4.4	84.65	14.66	0.69	40.5	30.54	28.97	56.58	40.47	2.95
TP37	31.55	63.53	4.92	84.03	15.97	0	33.67	27.19	39.15	46.24	53.76	0
TP302X	30.66	65.56	3.78	87.45	12.55	0	35.5	28.57	35.93	49.69	50.31	0
S112	35.03	60.36	4.6	84.8	15.2	0	38.67	29.34	31.99	54.73	45.27	0
TP38	31.52	66.77	1.71	92.13	7.87	0	39.39	0	60.61	39.39	60.61	0
AT22	32.35	64.86	2.79	90.48	9.52	0	58.98	0	41.02	58.98	41.02	0
YJ2-14	40.92	44.47	14.61	71.59	23.85	4.56	50.51	18.18	31.32	52.82	32.75	14.43
YJ1-4CH	42.71	51.26	6.03	83.15	14.24	2.62	42.74	27.64	29.62	47.28	32.77	19.95
YJ2-1	42.15	51.46	6.39	82.53	15.64	1.84	47.02	24.86	28.12	57.65	34.48	7.87
YJ2-3	34.93	60.49	4.59	87.15	12.24	0.61	34.67	31.3	34.03	47.43	46.56	6.01
YJ3	32.06	65.38	2.56	89.69	9.84	0.47	31.2	34.92	33.88	44.87	48.73	6.4
YJ3-1	40.63	52.36	7.01	80.3	17.08	2.62	50.24	22.14	27.62	57.44	31.58	10.97
YJ2-11X	44.71	50.36	4.94	82.09	16.39	1.52	45.4	29	25.6	60.36	34.04	5.6
SB1-3CH	43.04	51.28	5.68	83.94	13.89	2.17	50.97	22.31	26.72	59.14	31	9.86
SB1-4H	43.47	50.96	5.57	83.4	14.84	1.76	48.31	24.35	27.34	58.46	33.08	8.46
SB5	47.63	45.18	7.19	81.23	17.41	1.36	50.77	23.98	25.25	63.75	31.71	4.54
S7	40.07	52.15	7.78	79.6	15.91	4.5	46.07	16.99	36.94	45.13	36.18	18.69
SN4	47.32	46.88	5.8	73.9	17.68	8.42	42.59	24.5	32.92	45.21	34.95	19.84
SN5	19.41	39.44	41.15	19.21	49.27	31.52	6.53	21.28	72.19	5.24	58	36.76

Notes: nC_{5-7}, iC_{5-7}, and CyC$_{5-7}$: the relative abundances of *n*-alkanes, *iso*-alkanes and cycloalkanes of C_5–C_7 LHs; n + iC_{6-7}, CyC$_{6-7}$, and AroC$_{6-7}$: the relative abundances of (*n*- + *iso*-) alkanes, cycloalkanes, and aromatics of C_6–C_7 LHs; nC_7, DMCP, and MCH: the relative abundances of *n*-heptane, dimethylcyclopentane, and methylcyclohexane; nC_7, MCH, and Tol: the relative abundances of *n*-heptane, methylcyclohexane, and toluene; see Table 2 for the full names and parameter calculations of light hydrocarbons.

Shunnan area exhibits particularly high maturity, comparable to over-mature oil-cracking gases from the Anyue gas field, as evidenced by its position on the C_1 content versus dryness coefficient plot (Fig. 3(a)).

Oil-associated thermogenic gas can be generated both through the direct degradation of kerogen and the thermal cracking of crude oil (e.g., Prinzhofer and Huc, 1995; Prinzhofer and Battani, 2003). Hill et al. (2003) originally delineated three stages of oil cracking as C_{15}^{+} cracking dominant, C_6–C_{14} cracking dominant, and C_2–C_5 cracking dominant. Numerous studies (Chen et al., 2016; Pan et al., 2010, 2012; Tian et al., 2008, 2010, 2012) have employed a two-stage model characterized by the primary cracking of oil components into wet gas and the subsequent secondary cracking of wet gas into dry gas. Chen et al. (2016) notably identified preliminary low-temperature cracking of oil components, which resulted in a limited gas yield, aligning with the C_{15}^{+} cracking dominant stage delineated by Hill et al. (2003). More recently, Maimaiti et al. (2022) reintroduced a three-stage framework that includes the lightning of oil cracking (C_{14}^{+} cracking to C_6–C_{14}), the cracking of light components to wet gas (C_6–C_{14} cracking to C_2–C_5), and the cracking of wet gas (C_2–C_5 cracking to C_1). This mirrors the original three-stage classification proposed by Hill et al. (2003).

In this study, the gas samples exhibit a progressive increase in the values of ln (C_1/C_2) and ln (C_2/C_3) (Fig. 3(e)). This trend mirrors the evolutionary trend observed in oil cracking gases from the Anadarko Basin, Kansas (Prinzhofer and Huc, 1995), suggesting a transition from primary to secondary oil cracking. The SN5 well gas sample from Shunnan area occupies the position of a typical cracking dry gas from the Anyue gas field, indicating its classification within the stage of wet gas cracking (Stage III). Most gas samples from the Tahe East, Lunnan, Jilake, Shunnan, Shunxi, Tazhong, and Hetianhe areas, as well as gas samples from the ST1

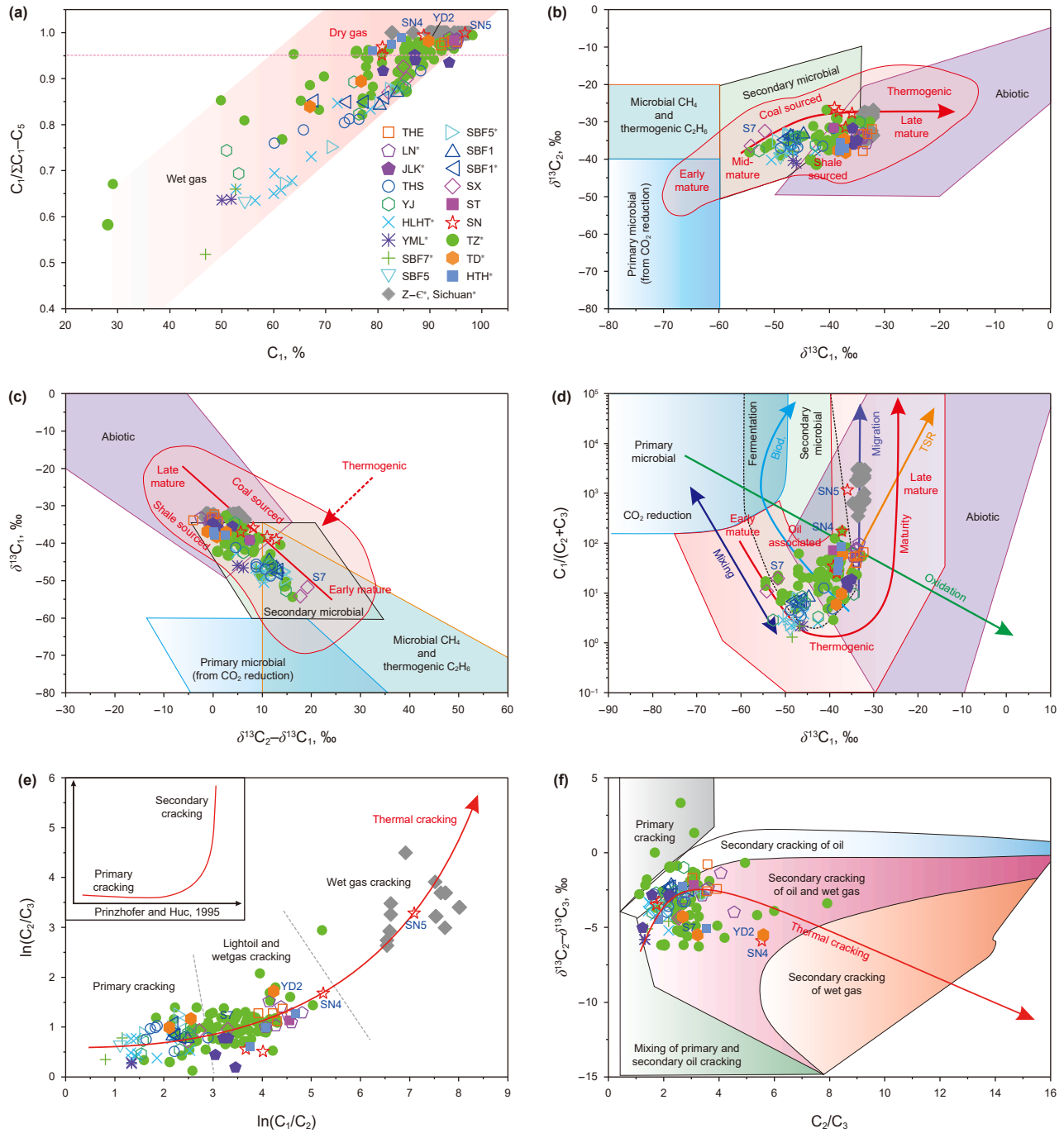

Fig. 3. Cross-plots showing the genesis of the deep natural gases in the Tarim Craton. **(a)** CH_4 content versus dryness coefficient ($C_1/\Sigma C_{1-5}$); **(b)** $\delta^{13}C_1$ versus $\delta^{13}C_2$ (after Milkov, 2021); **(c)** $\delta^{13}C_2$–$\delta^{13}C_1$ versus $\delta^{13}C_1$ (after Milkov, 2021); **(d)** $\delta^{13}C_1$ versus $C_1/(C_2+C_3)$ (after Milkov and Etiope, 2018); **(e)** ln (C_1/C_2) versus ln (C_2/C_3) (after Prinzhofer and Huc, 1995); and **(f)** C_2/C_3 versus $\delta^{13}C_2$–$\delta^{13}C_3$ (after Liu et al., 2018, 2019). *: Data from the literature; see Supplementary Table S1 for details.

well in the Shuntuo area and the YD2 well in the Tadong area, exhibit intermediate ln (C_1/C_2) and ln (C_2/C_3) values, thus defining them as being in the transitional cracking stage (Stage II) associated with crude oil and wet gas cracking. Meanwhile, gases from the Shunbei, Yingmaili, Tahe South, and Yuejin areas generally display low ln (C_1/C_2) and ln (C_2/C_3) values, which are characteristic of primary cracking (Stage I). It should be noted that the three-stage classification of crude oil thermal cracking established by Hill et al. is based on thermal simulation experiments conducted on a single oil phase. Under geological conditions, however, source rocks generate crude oil alongside varying amounts of kerogen degradation gas, leading to the co-accumulation of both oil and gas in reservoirs. Consequently, regardless of the extent of oil cracking, this kerogen-derived gas component persists in the reservoirs. During Stage I of crude oil cracking, the contribution of oil-cracking gas remains relatively low (Chen et al., 2016; Hill et al., 2003; Maimaiti et al., 2022), and natural gas in the reservoir is therefore dominated by kerogen-degradation gas. In contrast, during Stages II to III, oil-cracking gas constitutes a significantly higher proportion (Chen et al., 2016; Maimaiti et al., 2022).

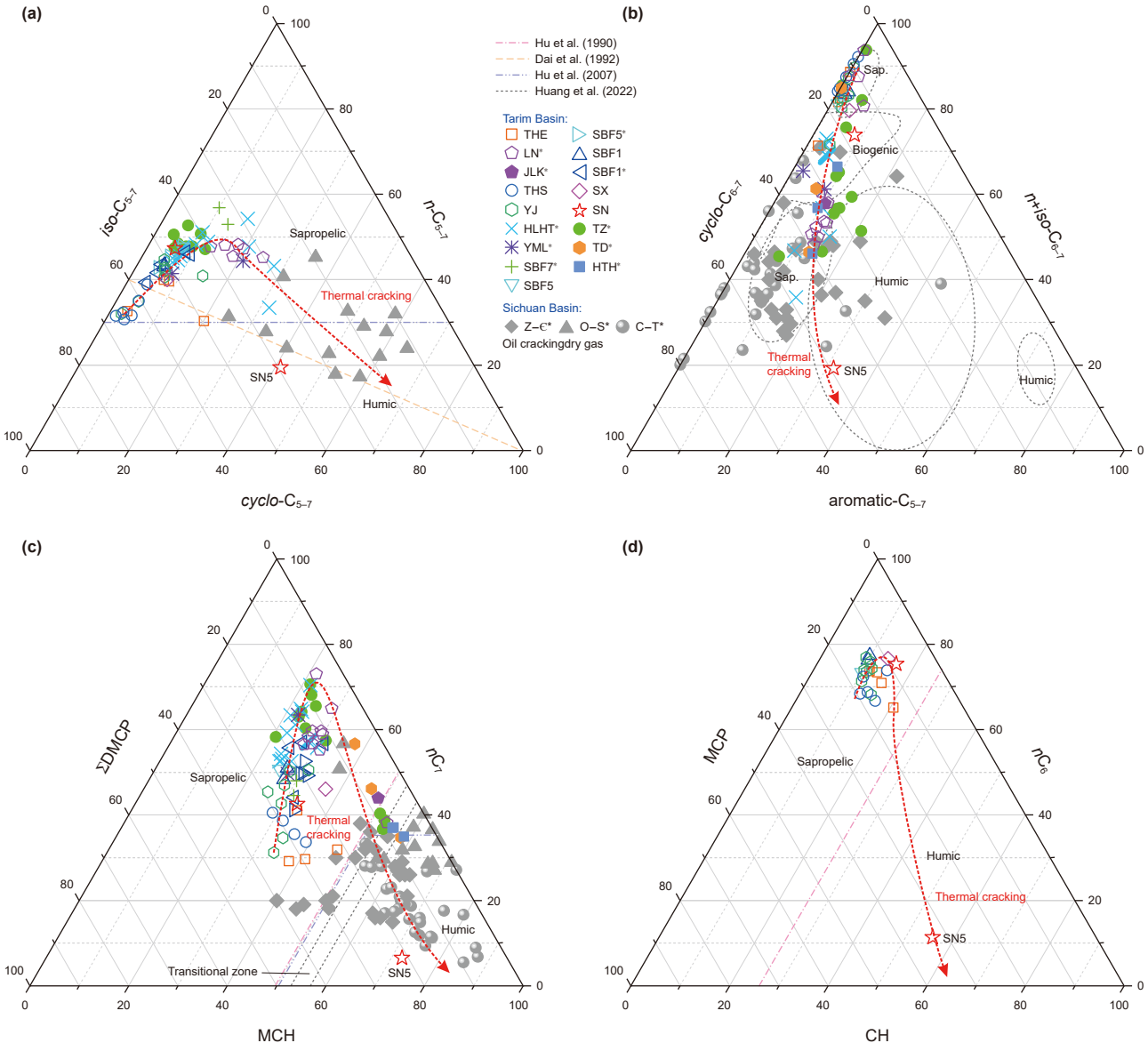

Fig. 4. Triangle diagrams showing the organic matter input of deep gases in the Tarim Craton. **(a)** triangle diagram of *n*-$C_{5–7}$, *iso*-$C_{5–7}$, and *cyclo*-$C_{5–7}$ (after Dai et al., 1992; Hu et al., 2007); **(b)** triangle diagram of *n* + *iso*-$C_{5–7}$, *cyclo*-$C_{5–7}$, and aromatic-$C_{5–7}$ (after Huang et al., 2022b); **(c)** triangle diagram of nC_7, ΣDMCP, and MCH (after Dai et al., 1992; Hu et al., 1990; Hu et al., 2007, 2008; Huang et al., 2022b); and **(d)** triangle diagram of nC_6, MCP, and CH (after Hu et al., 1990). *: Data from the literature, see Supplementary Table S2 for details.

Simultaneously, the previously accumulated kerogen degradation gas undergoes secondary cracking, ultimately resulting in oil-cracking gas as the dominant component in the reservoirs.

The C_2/C_3 and $\delta^{13}C_2$–$\delta^{13}C_3$ plot (Liu et al., 2018, 2019; Lorant et al., 1998; Prinzhofer and Battani, 2003) provides additional validation (Fig. 3(f)). Most samples are situated within the secondary cracking zone, although the Shunnan area SN5 well gas and Anyue gases could not be plotted due to low C_3 content and/or unavailability of $\delta^{13}C_3$ data, which is consistent with their wet gas cracking stage. Nonetheless, some primary cracking gases appear displaced into the secondary cracking zone, revealing limitations in this classification scheme. In summary, these oil-associated thermogenic gases originate predominantly from sapropelic organic matter and represent the complete thermal cracking continuum, making them ideal for characterizing LHs evolution throughout thermal maturation processes.

5.2. Influence of thermal cracking on LH parameters

5.2.1. Parameters related to organic matter types

The $C_{5–7}$ ternary diagram, which utilizes the relative abundances of *n*-alkanes, *iso*-alkanes and *cyclo*-alkanes, represents a well-established method for characterizing organic matter inputs in natural gas studies (Dai et al., 1992; Hu et al., 2007, 2008, 2014, 2017, 2018). In the present study, most gas samples plot within the sapropelic zone (Fig. 4(a)), indicating derivation from sapropelic organic matter. The exception is the Shunnan area SN5 well gas in the Tarim Basin and most oil-cracking dry gases from the Sichuan Basin, which are plotted in the humic zone despite their known sapropelic origin. Examination of thermal cracking levels progressive enrichment of $nC_{5–7}$ during early cracking stages (Stages I–II) without altering organic matter type identification. However, advanced cracking (Stage III) results in significant *cyclo*-alkane

enrichment that may lead to misclassification of organic matter types.

For organic matter type classification based on *chain*-alkanes (*n*- + *iso*-), *cyclo*-alkanes, and aromatics, the C_{6-7} fraction is typically employed. Leythaeuser et al. (1979a, 1979b) demonstrated that humic gases contain more than 27% C_{6-7} aromatics, while sapropelic gases contain less than 5%. Dai et al. (1992) further established that humic gases generally have less than 17% C_{6-7} aliphatic (*chain*- and *cyclo*-alkanes) content, in contrast to sapropelic gases, which exceed this threshold. More recently, Huang et al. (2022b) illustrated the distribution of gases from various origins using a triangular diagram (Fig. 4(b)), derived from an extensive dataset of global samples. In this study, the majority of samples plot within the sapropelic zones, attributed to their low aromatic content, which is consistent with their thermogenic derivation from sapropelic organic matter. Notably, gas samples that have undergone extensive thermal cracking (e.g., gas from the Shunnan area SN5 well of the Tarim Basin and certain samples from the Sichuan Basin) anomalously appear in the humic zone, reflecting aromatics enrichment during advanced cracking, rather than true humic origin. Additionally, some samples plot in the biogenic field, likely representing mixing between biogenic and sapropelic gases rather than pure biogenic gas.

The nC_7–ΣDMCP–MCH ternary diagram also serves as a key tool for organic matter type classification in natural gas research (Hu et al., 1990; Hu et al., 2007, 2008; Huang et al., 2022a,b). As shown in Fig. 4(c), most samples in this study plot within the sapropelic zone, consistent with their sapropelic organic matter origin. However, severely cracked gases (e.g., a sample from the SN5 well of the Shunnan area, Tarim Basin and most samples from the Sichuan Basin) anomalously plot in the humic zone due to MCH enrichment exceeding 57%, reflecting advanced thermal alteration rather than true humic origin.

The nC_6–MCP–CH ternary diagram, though less commonly used, provides valuable supplementary information for organic matter type classification (Zhang et al., 2025). Hu et al. (1990) determined, through analysis of Chinese samples, that humic gases typically contain more than 27% ± 2% CH, while sapropelic gases contain less than 27% ± 2% CH. In this study, most samples plot within the sapropelic zone (Fig. 4(d)), consistent with their geological origins. The SN5 gas sample anomalously appears in the humic zone, demonstrating that severe thermal cracking can lead to organic matter type misclassification when using this diagram.

5.2.2. Parameters related to source rock lithology

The molecular composition of C_7 hydrocarbons serves as a reliable indicator for distinguishing source rock lithologies. Conventional ternary diagrams utilizing 3RP (*iso*-C_7), 5RP (ΣDMCP), and 6RP (MCH + Tol) reveal distinct compositional patterns: lacustrine-sourced oils typically show 3RP predominance, marine-sourced oils exhibit 5RP dominance, and terrigenous oils display 6RP prevalence, though with notable overlap between categories (Ten Haven, 1996). Subsequent methodological refinements include the substitution of (2- + 3-) MH for 3RP (Odden et al., 1998) and the replacement of both 3RP and 5RP with (2- + 3-) MH and ΣDMCP+ΣDMP, respectively (Obermajer et al., 2000). In this study, marine-sourced gases from the Tarim Craton demonstrate predominant 3RP and 5RP signatures, with significantly higher (2- + 3-) MH and 5RP contents compared to Mid-Norway marine shales (Fig. 5(a) and (b)). Gas from the SN5 well in the Shunnan area represents a notable exception, exhibiting exclusive 3RP dominance that closely resembles Mid-Norway coal and paralic shale compositions. This anomalous signature likely results from extensive thermal cracking, which induces 3RP enrichment and may lead to misinterpretation of source rock facies.

The alternative classification approach provides complementary insights. Jarvie et al. (2001, 2002) developed a ternary diagram incorporating nC_7, (*iso*-C_7 + ΣDMCP + EP), and (Tol + MCH) to differentiate marine shale, carbonate, and kukersite oil shale in the Williston Basin. Kukersite shale, an Ordovician marine Type I kerogen shale, is characterized by abundant algal remains of Gloeocapsomorpha prisca. Hill et al. (2007) subsequently modified this approach by creating a revised ternary diagram using nC_7, Tol, and MCH to address overlapping signatures between terrigenous and carbonate sources in previous systems. Application of these classification schemes to Tarim Craton samples yields consistent results. Most gas samples plot within the marine shale field (Fig. 5(c) and (d)), confirming the Lower Cambrian marine shale as the primary hydrocarbon source (Cai et al., 2009, 2015; Sun et al., 2025; Zhu et al., 2021). The gas sample from the Shunnan area SN5 well in the Tarim Basin and most gas samples from the Sichuan Basin show marked deviations due to elevated (MCH + Tol) concentrations, demonstrating how advanced thermal cracking can compromise lithological interpretations.

Hill et al. (2007) demonstrated that organic matter quality exerts greater control on molecular signatures than lithology alone. This explains the substantially higher 5RP and (2- + 3-) MH contents in Tarim samples compared to Spekk Formation references (Odden et al., 1998), reflecting the superior organic matter quality (Type I to II kerogen) of Lower Cambrian source rocks versus the Type II to III kerogen of the Spekk Formation.

5.2.3. Parameters related to gas–gas correlation

The C_7 star methodology, originally developed by Halpern (1995) and subsequently applied in numerous studies (e.g., Lerch et al., 2016; Wever, 2000), provides an effective approach for comparing oil and gas origins through five principal indices (C1 to C5; see Table 2 for definitions). The studied samples reveal that, while C3 values remain relatively consistent across all gas samples, distinct compositional patterns emerge in other indices. The Shunnan area SN5 well gas exhibits notably low C2, high C1, and high C4 values. In contrast, the Shunan area SN4 well, the Shunxi area S7 well, and the Tahe East area DK25-1 well gases demonstrate intermediate values for these indices, while the remaining samples are characterized by high C2, low C1, and low C4 values (Fig. 6(a)). These variations suggest that moderate to advanced thermal cracking (Stage II to III) can significantly alter C1, C2, and C4 values, potentially compromising the reliability of genetic comparisons using this methodology.

The catalytic theory introduced by Mango (1987, 1990, 1992, 2000) classifies C_7 LHs into parent (e.g., P_2 and P_3) and daughter (e.g., N_1 and N_2) species, proposing that petroleum from common sources maintains consistent reaction rates (e.g., K_1 and K_2). These parameters have been widely adopted in comparative studies (Huang et al., 2022a, 2023; Wu et al., 2014a). Here, the K_1 values of the studied samples ranged from 0.95 to 1.17 (Fig. 6(b)). These values correspond closely with, or slightly exceed, the globally recognized standard of 1.0 (Mango, 2000; Peters et al., 2005), indicating that thermal cracking exerts minimal influence on K_1. However, thermal cracking significantly affects K_2 values, as demonstrated by the wide range observed in our samples (0.18–0.57; Fig. 6(b)). This parameter shows progressive increases with thermal cracking intensity, indicating its limited utility for genetic comparisons of gases formed through thermal cracking.

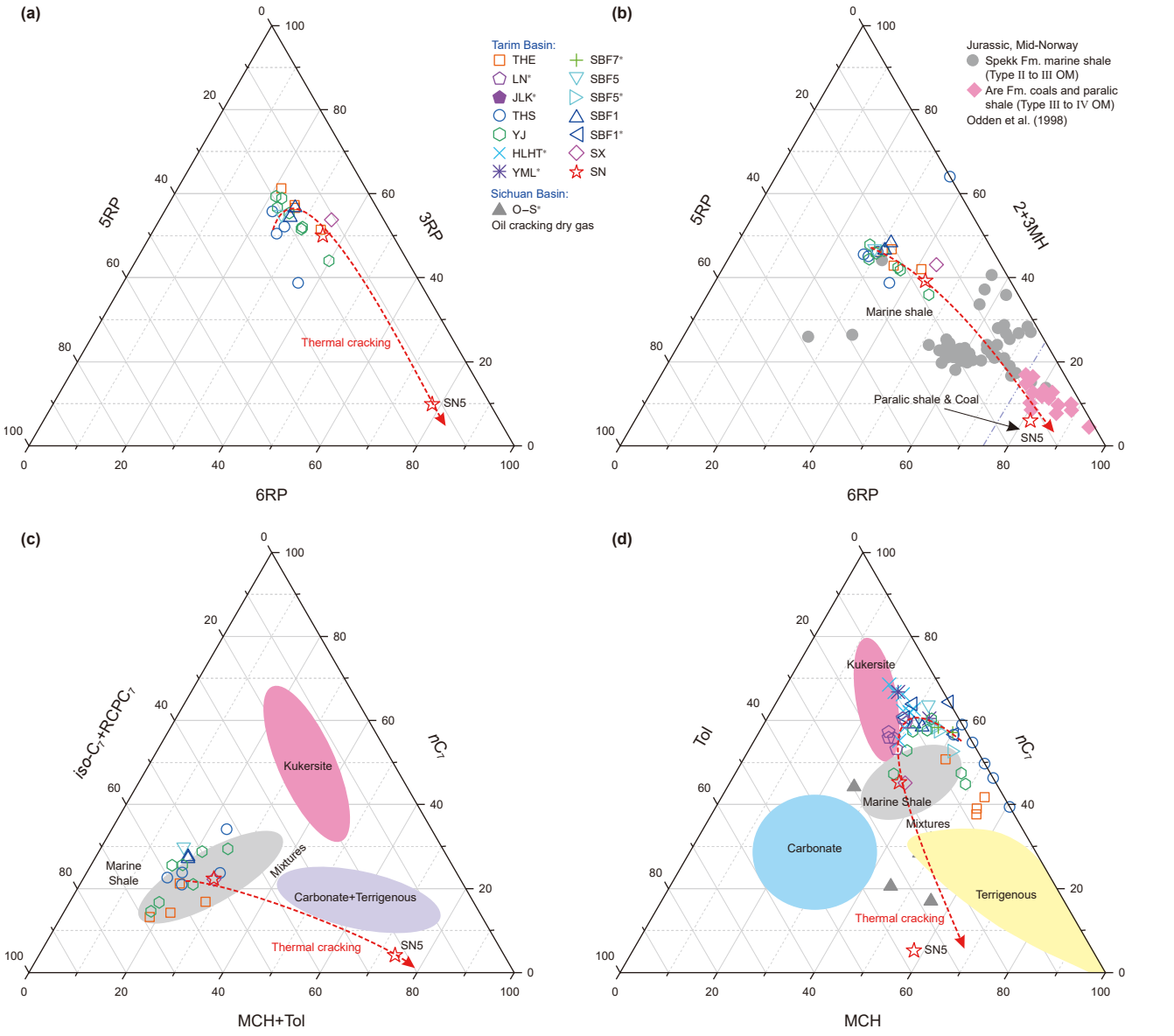

Fig. 5. Triangle diagrams showing the source rock facies of deep gases in the Tarim Craton. **(a)** triangle diagram of 3RP, 5RP, and 6RP (after Ten Haven, 1996); **(b)** triangle diagram of (2- + 3-) MH, 5RP, and 6RP (after Odden et al., 1998); **(c)** triangle diagram of nC_7, (*iso*-C_7 + $RCPC_7$), and (MCH + Tol) (after Jarvie et al., 2001, 2002); and **(d)** triangle diagram of nC_7, Tol, and MCH (after Hill et al., 2007). *: Data from the literature, see Supplementary Table S2 for details.

The differential response of K_1 and K_2 to thermal stress provides important insights into catalytic processes during hydrocarbon cracking.

5.2.4. Parameters related to thermal maturity

The commonly used formula [Ctemp = 140 + 15 ln (2,4-/2,3-DMP)] is employed to calculate oil and gas generation temperatures (BeMent et al., 1995; Mango and Hightower, 1997). Here, the 2,4-/2,3-DMP ratio emerges as a particularly robust maturity parameter, exhibiting stable and progressive increases with thermal cracking intensity (Fig. 7(a)). Additionally, the calculated temperatures for the studied samples are 132–144 °C. These values are significantly lower than current reservoir temperatures (150–200 °C; Qiao et al., 2024; Zhou et al., 2019) and known oil cracking thresholds (160–200 °C; Maimaiti et al., 2022; Qi et al., 2023; Zhu et al., 2021). Typically, deeper burial of source rocks results in reservoir temperatures being lower than generation temperatures. However, in deep petroleum systems, continuous subsidence of early-formed oil and gas reservoirs elevates formation temperatures, which may eventually exceed the initial generation temperatures. When reservoir temperatures remain below the thermal cracking threshold of crude oil, the original hydrocarbon composition is generally preserved. Under these conditions, the inferred generation temperature remains lower than the current reservoir temperature. In contrast, when reservoir temperatures exceed the oil-cracking threshold, extensive thermal conversion of oil to gas occurs, leading to comparable values between the inferred generation temperature and the reservoir temperature. Considering this, for gas samples from the Shunbei and Yuejin areas, the calculated temperatures likely reflect kerogen degradation rather than oil cracking, whereas for gas samples from the Shunnan area, the formula's derivation from kerogen-degradation gases limits its reliability as crude oil cracking becomes dominant. These results validate the 2,4-/2,3-DMP ratio as an effective maturity indicator, while also highlighting the need for recalibrated temperature relationships.

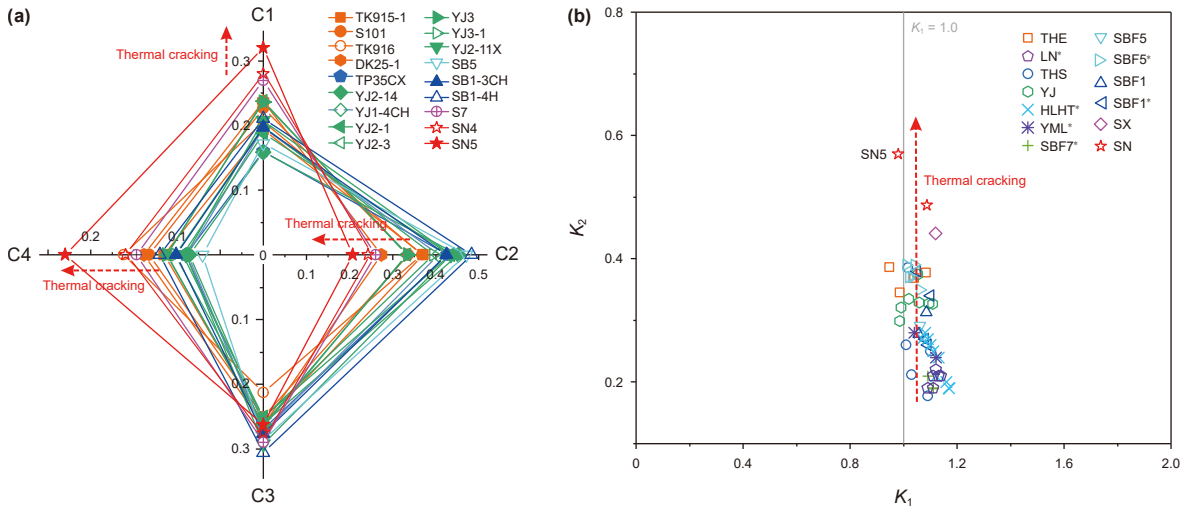

Fig. 6. Diagrams showing the gas correlations of deep gases in the Tarim Craton. **(a)** C_7 gas comparison star diagram (after Halpern, 1995); and **(b)** cross-plot of K_1 versus K_2. *: Data from the literature, see Supplementary Table S2 for details.

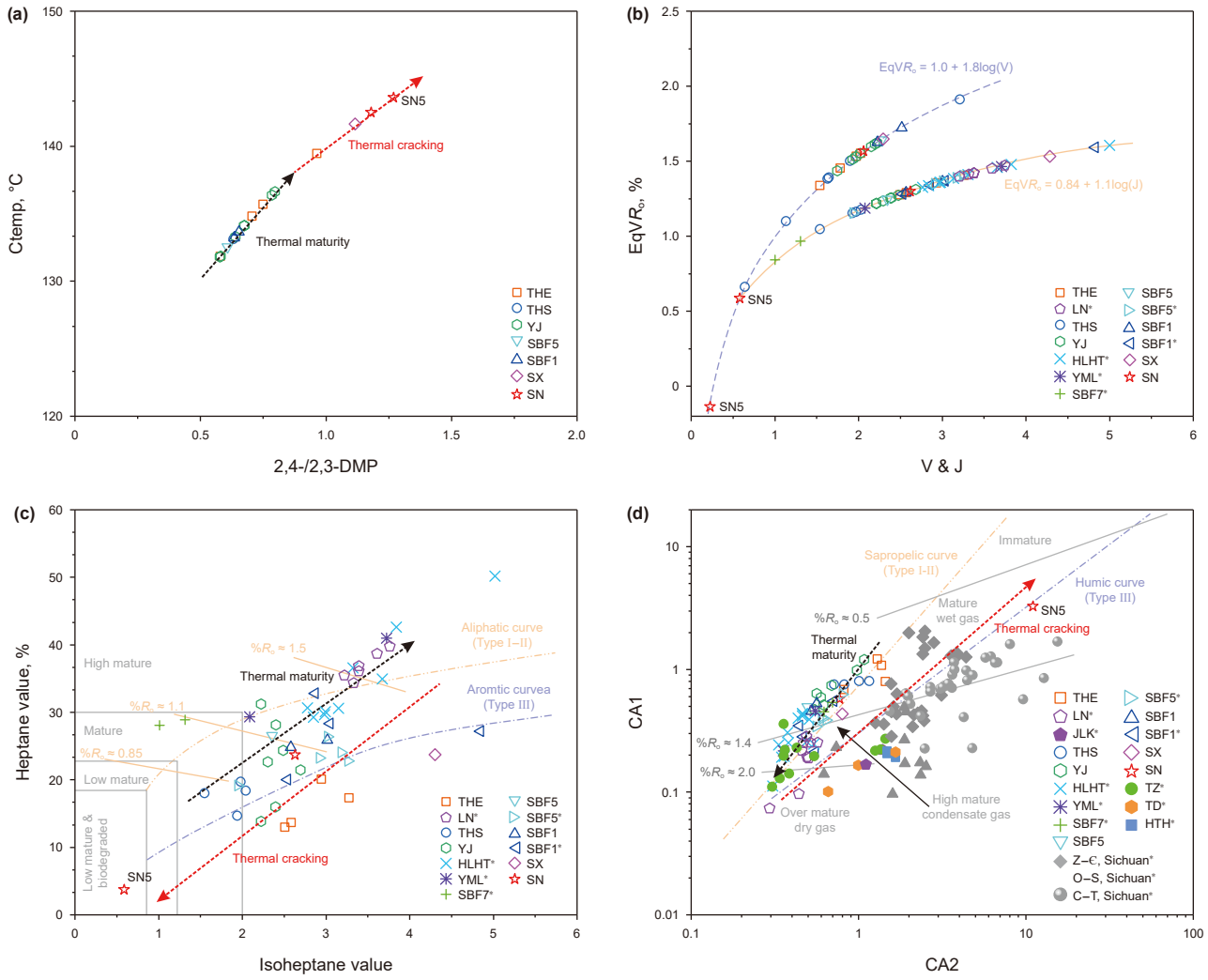

Fig. 7. Cross-plots showing the thermal maturity of deep gases in the Tarim Craton. **(a)** 2,4-/2,3-DMP versus Ctemp, Ctemp = 140 + 15 ln (2,4-/2,3-DMP) (BeMent et al., 1995; Mango and Hightower, 1997); **(b)** V and J versus EqVR_o, EqVR_o = 1.0 + 1.8 log(V) and EqVR_o = 0.84 + 1.1 log(J) (Schaefer and Littke, 1988); **(c)** H versus I (after Thompson, 1987; Walters et al., 2003); and (d) CA2 versus CA1 (after Hu et al., 1990). *: Data from the literature, see Supplementary Table S2 for details.

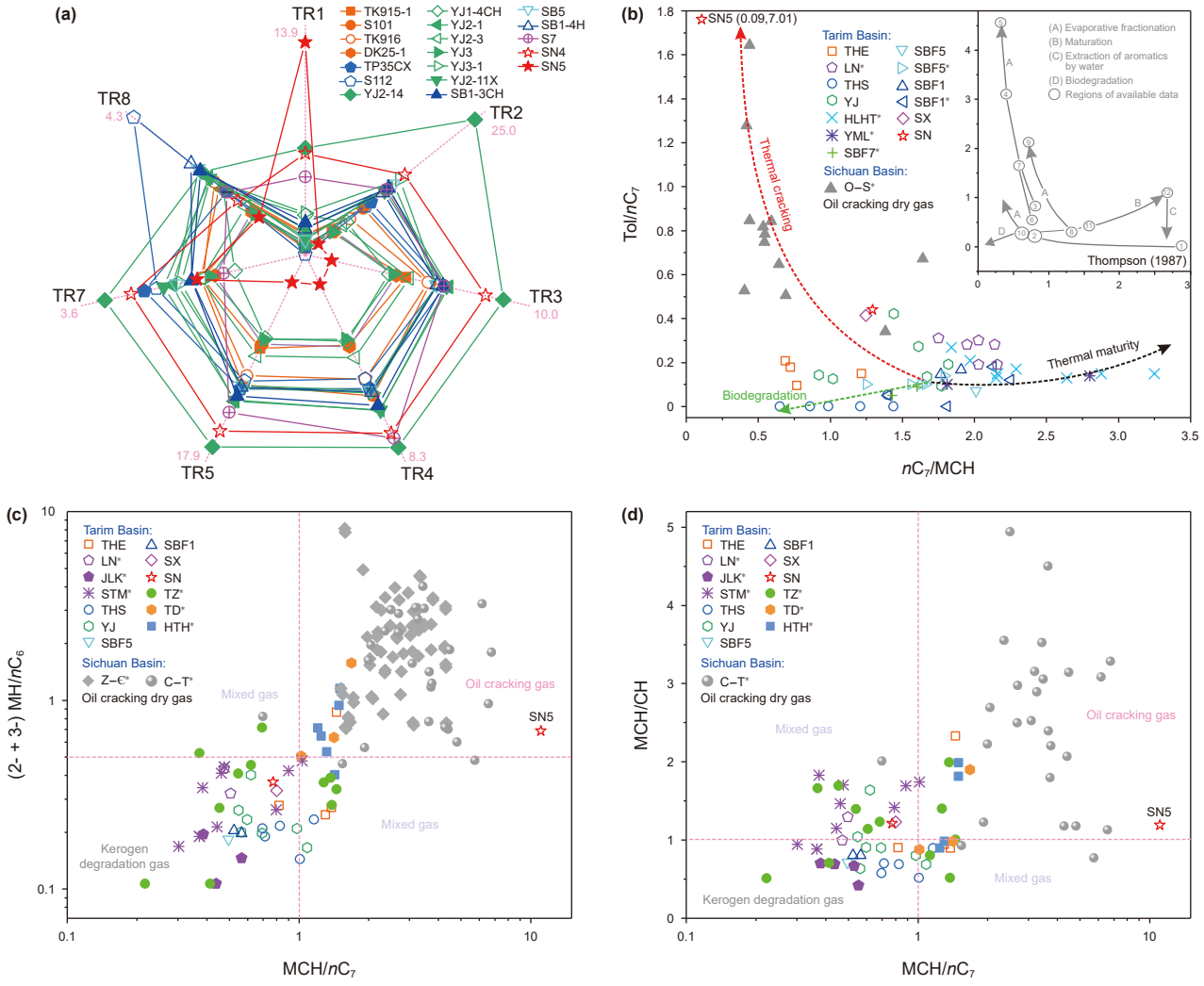

Fig. 8. Diagrams showing the secondary alteration of deep natural gases in the Tarim Craton. **(a)** C_7 gas alteration star diagram (after Halpern, 1995); **(b)** nC_7/MCH (F) versus Tol/nC_7 (B) (after Thompson, 1987); **(c)** MCH/nC_7 versus [(2- + 3-) MH]/nC_6 (after Hu et al., 2005, 2018); and **(d)** MCH/nC_7 versus MCH/CH (after Hu et al., 2005, 2018). *: Data from the literature, see Supplementary Table S2 for details.

The established thermal stability sequence of light hydrocarbons (aromatics > *n*-alkanes > *iso*-alkanes > *cyclo*-alkanes; Hu et al., 1990; Huang et al., 2022b; Philippi, 1975; Thompson, 1979, 1983, 1987) has enabled the development of multiple maturity indices. Philippi (1975) introduced the C_7 *chain*-/*cyclo*-alkane ratio, while Thompson (1979, 1983) expanded the suite to include nC_7/MCH (F), heptane value (H), and isoheptane value (I). Schaefer and Littke (1988) subsequently proposed the equations $EqVR_o = 1.0 + 1.8\log(V)$ and $EqVR_o = 0.84 + 1.1\log(J)$, where $EqVR_o$ is the abbreviation for equivalent vitrinite reflectance, V represents the C_7 *chain*-/*cyclo*-alkane ratio and J corresponds to I. Analysis of Chinese basin samples by Hu et al. (1990) revealed that, while H and I proved ineffective as maturity indicators, alternative parameters including RCPC$_7$/nC_7 (CA1), MCH/nC_7 (CA2), and C_7 *cyclo*-alkane/paraffin (CA3) showed negative correlations with thermal maturation, with CA2 and CA3 serving as inverse proxies for F and V, respectively.

In this study, the calculated $EqVR_o$ values from V range from 0.66% to 1.94%, with SN5 as an outlier (−0.14%). For parameter J, $EqVR_o$ values range from 0.84% to 1.61%, again with SN5 well gas as an outlier (0.59%) (Fig. 7(b)). These findings indicate parameter inversion during severe cracking stages. The H versus I maturity plot (Fig. 7(c)) positions most samples in the mature-to-high-mature zone, with the Shunnan area SN5 well sample anomalously plotting in the low-maturity region. Samples from the SN4 well in the Shunnan area, as well as the Yuejin, Shunxi, and Tahe East areas, exhibit depressed H and I values near the aromatic (humic) curve despite their high maturity, suggesting that thermal cracking alters these indices. Similarly, the CA1 versus CA2 plot shows most samples in the mature to over-mature zone (Fig. 7(d)), with the SN5 well sample from Shunnan area again deviating. Notably, the samples from the Tarim Craton appear more mature than Sichuan Basin cracked gases, contrary to expectations. Meanwhile, several samples from the Shunnan area SN5 well and the Lunnan, Jilake, Tadong, Hetianhe, and Tazhong areas in the Tarim Craton, as well as most Sichuan Basin gases, align with the humic curve despite their sapropelic origin, further demonstrating index inversion during thermal cracking.

5.2.5. Parameters related to secondary alteration

Halpern (1995) established a C_7 star diagram incorporating eight alteration indices (TR1–TR8; see Table 2 for definitions) that exhibit progressively decreasing sensitivity to biodegradation processes. Among these parameters, TR1 and TR6 specifically indicate water washing and evaporation fractionation,

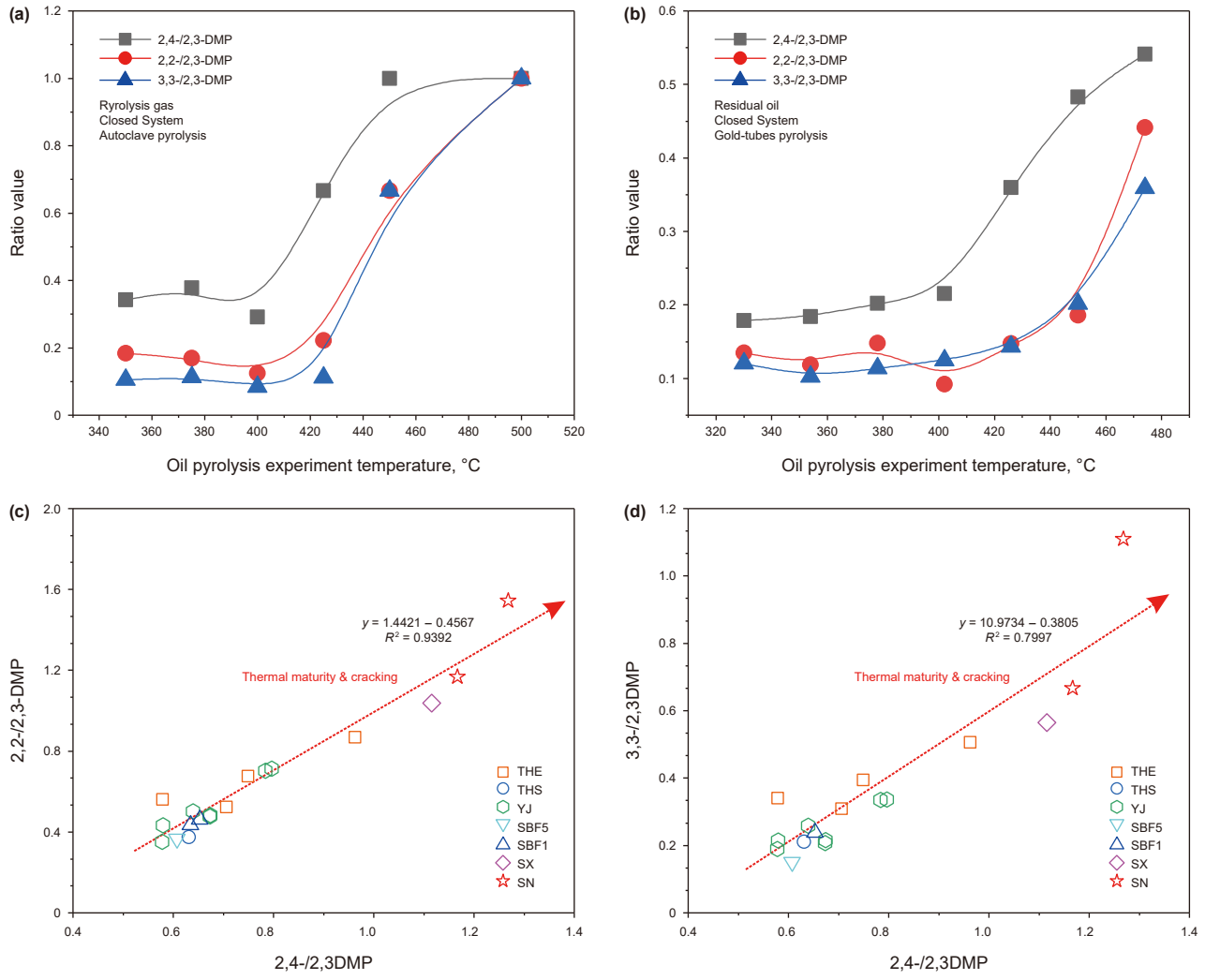

Fig. 9. Diagrams showing the changes in the ratios of 2,2-/2,3-, 2,4-/2,3-, and 3,3-/2,3-DMP during the thermal cracking and thermal maturation. **(a)** Cross-plot of 2,4-/2,3-, 2,2-/2,3-, and 3,3-/2,3-DMP vs. experimental temperature of the pyrolysis gas (data from Chai et al., 2026); **(b)** cross-plot of 2,4-/2,3-, 2,2-/2,3-, and 3,3-/2,3-DMP vs. experimental temperature of the residual oil (data from Huang et al., 2022a, 2023); **(c)** cross-plot of 2,2-/2,3-DMP vs. 2,4-/2,3-DMP of deep gases in the Tarim Craton; and **(d)** cross-plot of 3,3-/2,3-DMP vs. 2,4-/2,3-DMP of deep gases in the Tarim Craton. See Table 2 for full names of LHs.

respectively (Halpern, 1995; Peters et al., 2005). The Shunnan area SN5 well gas sample demonstrates a distinctive compositional signature characterized by significantly elevated TR1 values and reduced TR2–TR8 values compared to those of other samples (Fig. 8(a)). This pattern indicates that thermal cracking substantially influences star diagram parameters. Most other samples show a broader distribution of TR2–TR8 values, likely reflecting combined effects of thermal cracking and other geological processes. These observations demonstrate that thermal alteration can significantly modify diagnostic features of the C_7 star diagram.

Thompson (1987) established that evaporative fractionation preferentially depletes *n*-alkanes while enriching aromatic compounds and *cyclo*-alkanes. Consequently, aromatic to *n*-alkanes ratios (Bz/nC_6, Tol/nC_7, and (m + p)-xylene/nC_8) tend to increase with greater evaporative fractionation. However, these indices are also influenced by water washing, which removes aromatics, and thermochemical sulfate reduction, which enriches them (Thompson, 1983, 1987; Walters et al., 2015). The B-F diagram (Tol/nC_7 [B] versus nC_7/MCH [F]) serves as a valuable tool for assessing thermal maturity and identifying secondary alteration processes (Fig. 8(b) inset).

In this study, gas samples from the Tahe South area exhibit B values of 0 due to toluene absence (Fig. 8(b)), suggesting biodegradation. This is consistent with previous molecular marker studies (Chai et al., 2022; Wu et al., 2020). Samples from the Tahe East, Lunnan, Yuejin, Halahatang, Shunxi, and Shunnan areas in the Tarim Basin, as well as most samples from the Sichuan Basin, display elevated B values, with the highest values in the Sichuan Basin samples indicating possible evaporative fractionation. However, the anomalously high B values in the Shunnan area SN5 well and severely cracked Sichuan Basin gases more likely result from thermal cracking rather than evaporative fractionation, as the latter process primarily affects residual oil rather than natural gas.

Several LH indices effectively differentiate kerogen degradation gases from oil cracking gases, including MCH/nC_7 (>1.0 for oil cracking), (2- + 3-) MH/nC_6 (>0.5 for oil cracking), and MCH/CH (>1.0 for oil cracking) (Hu et al., 2005, 2018; Zhang, 2008). As shown in Fig. 8(c) and (d), most Tarim Basin samples, including moderately cracked gases from the Shunxi area (SX7 well), Shunnan area (SN4 well), Lunnan area, and Jilake area, plot within the kerogen degradation zone. In contrast, severely cracked

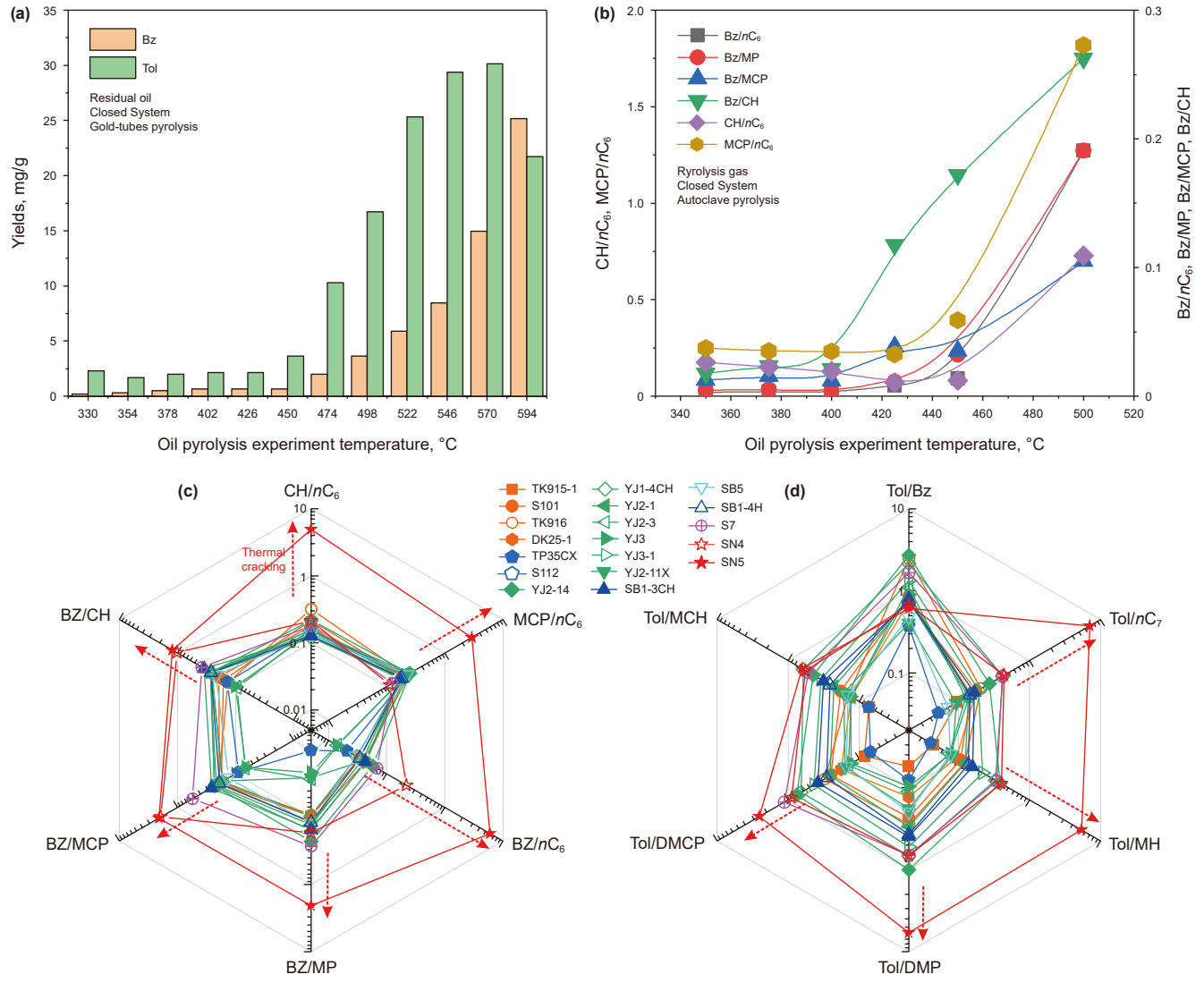

Fig. 10. Diagrams showing the variations of Bz and Tol yields and several LHs ratios during the thermal cracking. **(a)** Changes in the light aromatics (e.g., Bz and Tol) yields during the oil cracking experiment (data from Huang et al., 2022a, 2023); **(b)** changes in the ratios of Bz/nC_6, Bz/MP, Bz/MCP, Bz/CH, CH/nC_6, and MCP/nC_6 during the oil cracking experiment (data from Chai et al., 2026); **(c)** star diagram for Bz/nC_6, Bz/MP, Bz/MCP, Bz/CH CH/nC_6, and MCP/nC_6 ratios of deep gases in the Tarim Craton; **(d)** star diagram for Tol/Bz, Tol/nC_7, Tol/MH, Tol/DMP, Tol/DMCP, and Tol/MCH ratios of deep gases in the Tarim Craton.

samples from the Shunnan area SN5 well, Hetianhe area, Tadong area, Tahe East area, and Tazhong areas of the Tarim Basin, as well as Sichuan Basin dry gases, consistently fall within the oil cracking zone. These parameters show limited effectiveness for gases generated through mild-to-moderate oil cracking processes.

5.3. Novel potential indicators related to thermal maturity and thermal cracking

This study reveals that among LHs thermal maturity indices, only the 2,4-/2,3-DMP ratio maintains diagnostic efficacy under thermal cracking conditions (Fig. 7). Furthermore, commonly employed diagnostic ratios, including MCH/nC_7, MCH/CH, and (2- + 3-) MH/nC_6, demonstrate significant limitations in evaluating thermal cracking processes (Fig. 8(c) and (d)). These findings highlight the critical need to develop more robust geochemical proxies capable of accurately assessing both thermal maturity and cracking intensity.

Following the established pattern of the 2,4-/2,3-DMP maturity parameter, the ratios of 2,2-/2,3-DMP and 3,3-/2,3-DMP also exhibit systematic increases with thermal maturity and cracking intensity. As shown in Fig. 9(a), crude oil pyrolysis experiments conducted in an autoclave closed system demonstrate that these three ratios in pyrolysis gas generally rise with increasing temperature, particularly during high-temperature stages (>400 °C). Similarly, gold-tube closed-system pyrolysis experiments also show consistent increases in these ratios in residual oils with elevated temperatures, displaying a pronounced upward trend (Fig. 9(b)). Furthermore, analysis of deep natural gases from the Tarim Craton reveals clear correlations among 2,2-/2,3-DMP, 3,3-/2,3-DMP, and 2,4-/2,3-DMP ratios (Fig. 9(c) and (d)). These findings indicate that both 2,2-/2,3-DMP and 3,3-/2,3-DMP ratios can serve as reliable thermal maturity indicators, providing valuable complementary tools for high-maturity assessment, where traditional parameters often lose effectiveness.

Additionally, previous thermal simulation studies have elucidated systematic patterns in light aromatic stability during oil cracking processes. Al Darouich et al. (2006) conducted gold-tube pyrolysis experiments on light hydrocarbon fractions from non-biodegraded, marine-sourced Safaniya oil, demonstrating

progressive enrichment of light aromatics in residual oil with increasing pyrolysis temperature. Their results showed continuous benzene (Bz) enrichment across the temperature spectrum, while toluene (Tol) and xylene (Xyl) concentrations initially increased before declining under extreme thermal conditions. Complementary research by Huang et al. (2022a, 2023) on lacustrine-sourced Junggar Basin oils confirmed these general trends through similar pyrolysis experiments (Fig. 10(a)). Here, the analysis of the studied gas samples reveals consistent aromatic enrichment with increasing thermal stress, aligning closely with experimental pyrolysis results. The convergence of patterns between natural and experimental systems supports the potential of aromatic to aliphatic ratios as sensitive indicators for thermal maturity and cracking intensity assessment. Here, several aromatic-to-aliphatic ratios (e.g., Bz/nC_6, Bz/MP, Bz/MCP, Bz/CH, Tol/nC_7, Tol/MH, Tol/DMP, and Tol/DMCP) within the C_6–C_7 range were quantitatively analyzed. In pyrolysis gases derived from crude oil thermal cracking experiments, the Bz/nC_6, Bz/MP, Bz/MCP, and Bz/CH ratios increase systematically with temperature, particularly above 400 °C (Fig. 10(b)). Deep natural gases from the Tarim Craton show comparable trends, with severely cracked gas from the SN5 well exhibiting distinct values in the ratios of Bz/nC_6, Bz/MP, Bz/MCP, Bz/CH, Tol/nC_7, Tol/MH, Tol/DMP, and Tol/DMCP relative to those of other samples (Fig. 10(c) and (d)). Notably, the ratio of Bz/nC_6 demonstrates particularly strong diagnostic potential, effectively differentiating severely cracked (SN5 well gas), moderately cracked (SN4 well gas), and less altered natural gases. Similarly, *cyclo*-alkane to *n*-alkane ratios in the C_6 range (e.g., CH/nC_6 and MCP/nC_6) display elevated values at pyrolysis temperatures above 400 °C, effectively distinguishing natural gas from the Shunnan area SN5 well gas sample from other gas samples from the Tarim Craton. These systematic variations in these ratios highlight the utility of LH ratios as potential indicators for thermal maturity and cracking intensity evaluation.

6. Conclusions

(1) The deep natural gases within the Tarim Craton represent predominantly of thermogenic origin, spanning maturity stages from mature to over-mature, and are derived primarily from sapropelic organic matter in marine shale source rocks. Regional variations in gas composition reveal that the central Tabei Uplift and northern Shuntogole Low-Uplift contain mainly kerogen degradation gases, while the eastern Tabei Uplift, western Shuntogole Low-Uplift, Tazhong Uplift, and Hetianhe region are dominated by oil and wet gas cracking gases. Although the Shunnan area primarily contains crude oil and wet gas cracking gases, the SN5 well sample exhibits distinctive wet gas cracking characteristics that distinguish it from other samples.

(2) Severe thermal cracking, specifically wet gas cracking, produces anomalous enrichment of *cyclo*-alkanes and aromatics in light hydrocarbons, causing sapropelic gases to exhibit humic-type signatures. The genetic correlation index K_1 and the maturity indicator 2,4-/2,3-DMP remain effective across all cracking stages, while other parameters related to genetic correlations and maturity demonstrate reliability only for gases derived from initial cracking stages. Light hydrocarbon indicators related to secondary alteration undergo significant modification through thermal cracking processes. The ratios MCH/nC_7, (2- + 3-) MH/nC_6, and MCH/CH effectively distinguish between kerogen degradation gases and severely cracked gases but show limited resolution for initially cracked gases.

(3) Deep natural gases resulting from intense thermal cracking exhibit elevated ratios of *cyclo*-alkane to *n*-alkane in C_6 LHs and aromatic to aliphatic in C_6–C_7 LHs. These compositional characteristics highlight their potential as geochemical proxies for assessing thermal cracking intensity. The ratios 2,2-/2,3-DMP and 3,3-/2,3-DMP, similar to the established 2,4-/2,3-DMP parameter, show systematic increases with thermal stress, indicating their utility as reliable indicators of thermal maturity.

The diagnostic parameters proposed in this study, while substantiated through comprehensive analysis of available samples, require further validation using larger datasets to establish broader applicability. Although derived from a limited sample set, these findings establish significant preliminary frameworks and provide valuable insights for future research on thermal maturity and thermal cracking assessment in deep natural gas.

CRediT authorship contribution statement

Zhi Chai: Writing – original draft, Visualization, Methodology, Investigation, Formal analysis, Data curation. **Zhong-Hong Chen:** Writing – review & editing, Visualization, Supervision, Investigation, Formal analysis, Conceptualization. **Moïse Luemba:** Writing – review & editing, Validation, Software, Investigation. **Yong Chen:** Writing – review & editing, Project administration, Funding acquisition. **Fu-Lai Li:** Writing – review & editing, Software, Methodology, Data curation.

Declaration of competing interest

The authors declare that they have no known competing financial interests or personal relationships that could have appeared to influence the work reported in this paper.

Acknowledgement

This work is financed by the National Natural Science Foundation of China (Grant No. 42430808).

Appendix A. Supplementary data

Supplementary data to this article can be found online at https://doi.org/10.1016/j.petsci.2026.01.012.

References

Al Darouich, T., Behar, F., Largeau, C., 2006. Thermal cracking of the light aromatic fraction of Safaniya crude oil–experimental study and compositional modelling of molecular classes. Org. Geochem. 37 (9), 1130–1154. https://doi.org/10.1016/j.orggeochem.2006.04.003.

BeMent, W., Levey, R., Mango, F., 1995. The temperature of oil generation as defined with C_7 chemistry maturity parameter (2,4-DMP/2,3-DMP ratio). In: Grimalt, J.O., Dorronsoro, C. (Eds.), Org. Geochem., Development and Applications to Energy, Climate, Environment and Human History. DonostiaSan Sebastian, Spain: AIGOA, pp. 505–507.

Cai, C., Zhang, C., Cai, L., et al., 2009. Origins of Palaeozoic oils in the Tarim Basin: evidence from sulfur isotopes and biomarkers. Chem. Geol. 268, 197–210. https://doi.org/10.1016/j.chemgeo.2009.08.012.

Cai, C., Zhang, C., Worden, R., et al., 2015. Application of sulfur and carbon isotopes to oil–source rock correlation: a case study from the Tazhong area, Tarim Basin, China. Org. Geochem. 83, 140–152. https://doi.org/10.1016/j.orggeochem.2015.03.012.

Chai, Z., Chen, Z., Liu, H., et al., 2020. Light hydrocarbons and diamondoids of light oils in deep reservoirs of Shuntuoguole Low Uplift, Tarim Basin: implication for the evaluation on thermal maturity, secondary alteration and source characteristics. Mar. Petrol. Geol. 117, 104388. https://doi.org/10.1016/j.marpetgeo.2020.104388.

Chai, Z., Chen, Z., Patience, R., et al., 2022. Light hydrocarbons and diamondoids in deep oil from Tabei of Tarim Basin: implications on petroleum alteration and

mixing. Mar. Petrol. Geol. 138, 105565. https://doi.org/10.1016/j.marpetgeo.2022.105565.
Chai, Z., Chen, Z., 2023. Biomarkers, light hydrocarbons, and diamondoids of petroleum in deep reservoirs of the southeast Tabei Uplift, Tarim Basin: implication for its origin, alteration, and charging direction. Mar. Petrol. Geol. 147, 106019. https://doi.org/10.1016/j.marpetgeo.2022.106019.
Chai, Z., Chen, Z., Luemba, M., et al., 2026. Evolution and diagnostic potential of light hydrocarbons in thermally cracked gas: insights from crude oil pyrolysis experiments. Fuel 406, 136967. https://doi.org/10.1016/j.fuel.2025.136967.
Chen, F., Zhang, Y., Zhu, G., et al., 2018. Geochemistry and accumulation process of deep natural gas in the platform-basin region, Tarim Basin. Nat. Gas Geosci. 29 (6), 880–891. https://doi.org/10.11764/ji.ssn.1672-1926.2018.05.022 (in Chinese).
Chen, J., Miao, Z., Zhang, C., et al., 2010. Geochemical characteristics of light hydrocarbons in natural gas in the Tabei Uplift and their implications. Oil Gas Geol. 31 (3), 271–276 (in Chinese).
Chen, Z., Simoneit, B., Wang, T., et al., 2016. Effects of high temperatures on biomarker ratios during oil-to-gas cracking experiments at two pressures. Org. Geochem. 101, 108–131. https://doi.org/10.1016/j.orggeochem.2016.08.011.
Chen, Z., Wang, T., Li, M., et al., 2018. Biomarker geochemistry of crude oils and lower Paleozoic source rocks in the Tarim Basin, western China: an oil-source rock correlation study. Mar. Petrol. Geol. 96, 94–112. https://doi.org/10.1016/j.marpetgeo.2018.05.023.
Cheng, B., Liang, Y., Xu, J., et al., 2018. Remarkable fractionation of the hydrogen isotope (δD) of hydrocarbon during the fast aromatization process: insights from the pyrolysis experiments of *n*-butylcyclohexane. ACS Earth Space Chem. 2 (12), 1240–1248. https://doi.org/10.1021/acsearthspacechem.8b00111.
Dai, J., Pei, X., Qi, H., 1992. Natural Gas Geology of China. Petroleum Industry Press, Beijing, pp. 1–280 (in Chinese).
Feng, Z., Hao, F., Tian, J., et al., 2022. Shale gas geochemistry in the Sichuan Basin, China. Earth Sci. Rev. 232, 104141. https://doi.org/10.1016/j.earscirev.2022.104141.
Halpern, H., 1995. Development and application of light-hydrocarbon-based star diagrams. AAPG Bull. 79 (6), 801–815. https://doi.org/10.1306/8D2B1BB0-171E-11D7-8645000102C1865D.
He, M., Wang, Z., Moldowan, M., et al., 2022. Insights into catalytic effects of clay minerals on hydrocarbon composition of generated liquid products during oil cracking from laboratory pyrolysis experiments. Org. Geochem. 163, 104331. https://doi.org/10.1016/j.orggeochem.2021.104331.
He, S., Ma, A., Yun, L., et al., 2025. Organic geochemical characteristics and exploration significance of the Upper Ordovician Qrebake Formation source rocks, Shunbei area, Tarim Basin. Oil Gas Geol. 46 (1), 246–260. https://doi.org/10.11743/ogg20250117 (in Chinese).
Hill, R., Tang, Y., Kaplan, I., 2003. Insights into oil cracking based on laboratory experiments. Org. Geochem. 34 (12), 1651–1672. https://doi.org/10.1016/S0146-6380(03)00173-6.
Hill, R., Jarvie, D., Zumberge, J., et al., 2007. Oil and gas geochemistry and petroleum systems of the Fort Worth Basin. AAPG Bull. 91, 445–473. https://doi.org/10.1306/11030606014.
Hu, T., Ge, B., Zhang, Y., et al., 1990. The development and application of fingerprint parameters for hydrocarbons absorbed by source rocks and light hydrocarbons in natural gas. Exp. Pet. Geol. 12 (4), 375–394 (in Chinese).
Hu, G., Xiao, Z., Luo, X., et al., 2005. Light hydrocarbon composition difference between two kinds of cracked gases and its application. Nat. Gas. Ind. 25 (9), 23–25 (in Chinese).
Hu, G., Li, J., Li, J., et al., 2007. Discussion on the light hydrocarbons index in the identification of natural gas. Sci. China E D. 37 (1), 111–117 (in Chinese).
Hu, G., Li, J., Li, J., et al., 2008. Preliminary study on the origin identification of natural gas by the parameters of light hydrocarbon. Sci. China Earth Sci. 51, 131–139. https://doi.org/10.1007/s11430-008-5017-x.
Hu, G., Yu, C., Tian, X., 2014. The origin of abnormally high benzene in light hydrocarbons associated with the gas from the Kuqa depression in the Tarim Basin, China. Org. Geochem. 74, 98–105. https://doi.org/10.1016/j.orggeochem.2014.01.011.
Hu, G., Peng, W., Yu, C., 2017. Insight into the C_8 light hydrocarbon compositional differences between coal-derived and oil-associated gases. J. Nat. Gas Geosci. 2 (3), 157–163. https://doi.org/10.1016/j.jnggs.2017.08.001.
Hu, G., Li, J., Xie, Z., et al., 2018. Geochemistry of Light Hydrocarbon in Natural Gas. Petrol. Ind. Press, Beijing, pp. 1–281 (in Chinese).
Huang, Y., Liao, Y., Pan, Y., et al., 2022a. Improved light hydrocarbons collection method for the pyrolysis of crude oil in gold tube closed system experiments. Org. Geochem. 168, 104432. https://doi.org/10.1016/j.orggeochem.2022.104432.
Huang, Y., Liao, Y., Xu, T., et al., 2023. Characteristics of light hydrocarbons under the superimposed influence of biodegradation and subsequent thermal maturation. Org. Geochem. 177, 104557. https://doi.org/10.1016/j.orggeochem.2023.104557.
Huang, S., Li, J., Wang, T., et al., 2022b. Application of light hydrocarbons in natural gas geochemistry of gas fields in China. Annu. Rev. Earth Planet Sci. 50 (1), 13–53. https://doi.org/10.1146/annurev-earth-070921-054917.
Jarvie, D., Claxton, B., Henk, F., et al., 2001. Oil and shale gas from the Barnett Shale, Ft. Worth Basin, Texas (abs.). In: AAPG Annual Meeting Program, 10, A100.
Jarvie, D., McCaffrey, M., Mango, F., et al., 2002. Evaluation of petroleum systems with dual hydrocarbons charges: complementary application of light hydrocarbon, mid-range hydrocarbons, and biomarker assessments. In: Rangel, A., Goncalves, F., Parra, P., Hernández, C.M. (Eds.), 8th Latin-American Congress on Organic Geochemistry, October 20–24, 2002, Cartagena de Indias, Colombia: Latin American Association of Organic Geochemistry, Cartagena de Indias, pp. 50–52.
Jia, C., Wei, G., 2002. Structural characteristics and petroliferous features of Tarim Basin. Chin. Sci. Bull. 47, 1–11. https://doi.org/10.1007/BF02902812.
Jin, Z., Liu, Q., Yun, J., et al., 2017. Potential petroleum sources and exploration directions around the Manjar Sag in the Tarim Basin. Sci. China Earth Sci. 60 (2), 235–245. https://doi.org/10.1007/s11430-015-5573-7.
Leythaeuser, D., Schaefer, R., Cornford, C., et al., 1979a. Generation and migration of light hydrocarbons (C_2–C_7) in sedimentary basin. Org. Geochem. 1, 191–204. https://doi.org/10.1016/0146-6380(79)90022-6.
Leythaeuser, D., Schaefer, R., Weiner, B., 1979b. Generation of low molecular weight hydrocarbons from organic matter in source beds as a function of temperature and facies. Chem. Geol. 25, 95–108. https://doi.org/10.1016/0009-2541(79)90086-X.
Lerch, B., Karlsen, D., Abay, T., et al., 2016. Regional petroleum alteration trends in Barents Sea oils and condensates as a clue to migration regimes and processes. AAPG Bull. 100, 165–190. https://doi.org/10.1306/08101514152.
Liu, Q., Jin, Z., Li, H., et al., 2018. Geochemistry characteristics and genetic types of natural gas in central part of the Tarim Basin, NW China. Mar. Petrol. Geol. 89, 91–105. https://doi.org/10.1016/j.marpetgeo.2017.05.002.
Liu, Q., Wu, X., Wang, X., et al., 2019. Carbon and hydrogen isotopes of methane, ethane, and propane: a review of genetic identification of natural gas. Earth Sci. Rev. 190, 247–272. https://doi.org/10.1016/j.earscirev.2018.11.017.
Lorant, F., Prinzhofer, A., Behar, F., et al., 1998. Carbon isotopic and molecular constraints on the formation and the expulsion of thermogenic hydrocarbon gases. Chem. Geol. 147 (3–4), 249–264. https://doi.org/10.1016/S0009-2541(98)00017-5.
Ma, A., Li, H., Li, J., et al., 2020. Geochemical characteristics of Middle-Upper Ordovician source rocks in the Kalpin outcrop profiles and marine oil-source correlation, Tarim Basin, NW China. J. Nat. Gas Geosci. 5 (3), 143–155. https://doi.org/10.1016/j.jnggs.2020.04.001.
Ma, A., He, Z., Yun, L., et al., 2021. The geochemical characteristics and origin of Ordovician ultra-deep natural gas in the North Shuntuoguole area, Tarim Basin, NW China. J. Nat. Gas Geosci. 6 (5), 289–300. https://doi.org/10.1016/j.jnggs.2021.09.004.
Mango, F., 1987. An invariance in the isoheptanes of petroleum. Science 273, 514–517. https://doi.org/10.1126/science.237.4814.514.
Mango, F., 1990. The origin of light cycloalkanes in petroleum. Geochem. Cosmochim. Acta 54 (1), 23–27. https://doi.org/10.1016/0016-7037(90)90191-M.
Mango, F., 1992. Transition metal catalysis in the generation of petroleum and natural gas. Geochem. Cosmochim. Acta 56 (1), 553–555. https://doi.org/10.1016/0016-7037(92)90153-A.
Mango, F., Hightower, J., 1997. The catalytic decomposition of petroleum into natural gas. Geochem. Cosmochim. Acta 61 (24), 5347–5350. https://doi.org/10.1016/S0016-7037(97)00310-4.
Mango, F., 2000. The origin of light hydrocarbons. Geochem. Cosmochim. Acta 64 (7), 1265–1277. https://doi.org/10.1016/S0016-7037(99)00389-0.
Maimaiti, A., Wang, Q., Hao, F., et al., 2022. Oil pyrolysis with carbonate minerals: implications for the thermal stability of deep crude oil. Mar. Petrol. Geol. 146, 105929. https://doi.org/10.1016/j.marpetgeo.2022.105929.
Milkov, A., Etiope, G., 2018. Revised genetic diagrams for natural gases based on a global dataset of >20,000 samples. Org. Geochem. 125, 109–120. https://doi.org/10.1016/j.orggeochem.2018.09.002.
Milkov, A., 2021. New approaches to distinguish shale-sourced and coal-sourced gases in petroleum systems. Org. Geochem. 158, 104271. https://doi.org/10.1016/j.orggeochem.2021.104271.
Obermajer, M., Osadetz, K., Fowler, M., et al., 2000. Light hydrocarbon (gasoline range) parameter refinement of biomarker-based oil–oil correlation studies: an example from Williston Basin. Org. Geochem. 31 (10), 959–976. https://doi.org/10.1016/S0146-6380(00)00114-5.
Odden, W., Patience, R., van Grass, G., 1998. Application of light hydrocarbons (C_4–C_{13}) to oil/source rock correlation: a study of the light hydrocarbon compositions of source rocks and test fluids from offshore Mid-Norway. Org. Geochem. 28 (12), 823–847. https://doi.org/10.1016/S0146-6380(98)00039-4.
Pan, C., Jiang, L., Liu, J., et al., 2010. The effects of calcite and montmorillonite on oil cracking in confined pyrolysis experiments. Org. Geochem. 41 (7), 611–626. https://doi.org/10.1016/j.orggeochem.2010.04.011.
Pan, C., Jiang, L., Liu, J., et al., 2012. The effects of pyrobitumen on oil cracking in confined pyrolysis experiments. Org. Geochem. 45, 29–47. https://doi.org/10.1016/j.orggeochem.2012.01.008.
Peters, K., Walters, C., Moldowan, J., 2005. The Biomarker Guide, Vol. 1: Biomarkers and Isotopes in the Environment and Human History, second ed. Cambridge Univ. Press, New York.
Philippi, G., 1975. The deep subsurface temperature-controlled origin of the gaseous and gasoline-range hydrocarbons of petroleum. Geochem. Cosmochim. Acta 39, 1353–1373. https://doi.org/10.1016/0016-7037(75)90115-5.
Prinzhofer, A., Huc, A., 1995. Genetic and post-genetic molecular and isotopic fractionations in natural gases. Chem. Geol. 126, 281–290. https://doi.org/10.1016/0009-2541(95)00123-9.
Prinzhofer, A., Battani, A., 2003. Gas isotopes tracing: an important tool for hydrocarbons exploration. Oil Gas Sci. Technol. Rev. IFP 58, 299–311. https://doi.org/10.2516/ogst:2003018.
Qiao, R., Li, M., Zhang, D., et al., 2024. Geochemistry and accumulation of the ultra-deep Ordovician oils in the Shunbei oilfield, Tarim Basin: coupling of reservoir secondary processes and filling events. Mar. Petrol. Geol. 167, 106959. https://doi.org/10.1016/j.marpetgeo.2024.106959.

Qi, Y., Cai, C., Sun, P., et al., 2023. Crude oil cracking in deep reservoirs: a review of the controlling factors and estimation methods. Pet. Sci. 20 (4), 1978–1997. https://doi.org/10.1016/j.petsci.2023.03.006.
Rakotoalimanana, D., Béhar, F., Bounaceur, R., et al., 2016a. Thermal cracking of *n*-butylcyclohexane at high pressure (100 bar)—Part 1: experimental study. J. Anal. Appl. Pyrolysis 117, 1–16. https://doi.org/10.1016/j.jaap.2015.11.009.
Rakotoalimanana, D., Bounaceur, R., Béhar, F., et al., 2016b. Thermal cracking of *n*-butylcyclohexane at high pressure (100 bar)—Part 2: mechanistic modeling. J. Anal. Appl. Pyrolysis 120, 174–185. https://doi.org/10.1016/j.jaap.2016.05.003.
Schaefer, R., Littke, R., 1988. Maturity-related compositional changes in the low-molecular-weight hydrocarbon fraction of Toarcian shales. Org. Geochem. 13 (4–6), 887–892. https://doi.org/10.1016/0146-6380(88)90242-2.
Sun, P., Cai, C., Wang, D., et al., 2025. Unraveling the origin and charge of Halahatang oils. Tarim Basin. Org. Geochem. 204, 104962. https://doi.org/10.1016/j.orggeochem.2025.104962.
Tang, X., Huang, G., Zhang, M., 2019. Composition and genetic analysis of natural gas in Mandong area, Tarim Basin. Northwest. Geol. 52 (3), 173–180. https://doi.org/10.19751/j.cnki.61-1149/p.2019.03.015 (in Chinese).
Ten Haven, H., 1996. Application and limitations of Mango's light hydrocarbon parameters in petroleum correlation studies. Org. Geochem. 24 (10–11), 957–976. https://doi.org/10.1016/S0146-6380(96)00091-5.
Thompson, K., 1979. Light hydrocarbons in subsurface sediments. Geochem. Cosmochim. Acta 43, 657–672. https://doi.org/10.1016/0016-7037(79)90251-5.
Thompson, K., 1983. Classification and thermal history of petroleum based on light hydrocarbons. Geochem. Cosmochim. Acta 47, 303–316. https://doi.org/10.1016/0016-7037(83)90143-6.
Thompson, K., 1987. Fractionated aromatic petroleums and generation of gas-condensates. Org. Geochem. 11 (6), 573–590. https://doi.org/10.1016/0146-6380(87)90011-8.
Tian, H., Xiao, X., Wilkins, R., et al., 2008. New insights into the volume and pressure changes during the thermal cracking of oil to gas in reservoirs: implications for the in-situ accumulation of gas cracked from oils. AAPG Bull. 92 (2), 181–200. https://doi.org/10.1306/09210706140.
Tian, H., Xiao, X., Wilkins, R., et al., 2010. Genetic origins of marine gases in the Tazhong area of the Tarim basin, NW China: implications from the pyrolysis of marine kerogens and crude oil. Int. J. Coal Geol. 82, 17–26. https://doi.org/10.1016/j.coal.2010.01.012.
Tian, H., Xiao, X., Wilkins, R., et al., 2012. An experimental comparison of gas generation from three oil fractions: implications for the chemical and stable carbon isotopic signatures of oil cracking gas. Org. Geochem. 46, 96–112. https://doi.org/10.1016/j.orggeochem.2012.01.013.
Walters, C.C., Isaksen, G.H., Peters, K.E., 2003. Applications of light hydrocarbon molecular and isotopic compositions in oil and gas exploration. In: Hsu, C.S. (Ed.), Analytical Advances for Hydrocarbon Research. Modern Analytical Chemistry. Springer, Boston, MA.
Walters, C., Wang, F., Qian, K., et al., 2015. Petroleum alteration by thermochemical sulfate reduction—a comprehensive molecular study of aromatic hydrocarbons and polar compounds. Geochem. Cosmochim. Acta 153, 37–71. https://doi.org/10.1016/j.gca.2014.11.021.
Wang, Q., Xu, Z., Zhang, R., et al., 2024. New fields, new types of hydrocarbon explorations and their resource potentials in Tarim Basin. Acta Pet. Sin. 45 (1), 15–32. https://doi.org/10.7623/syxb202401002.
Wever, H., 2000. Petroleum and source rock characterization based on C_7 star plot results: examples from Egypt. AAPG Bull. 84, 1041–1054. https://doi.org/10.1306/A9673BA8-1738-11D7-8645000102C1865D.
Wu, Z., Chen, Z., Cao, Z., et al., 2020. Molecular marker and carbon isotope geochemistry of Ordovician oils in the Tuofutai Bulge, northern Tarim Basin: implications for oil maturity, source characteristics and filling directions. Mar. Petrol. Geol. 122, 104718. https://doi.org/10.1016/j.marpetgeo.2020.104718.
Wu, X., Liu, Q., Tao, X., et al., 2014a. Geochemical characteristics of natural gas from Halahatang Sag in the Tarim Basin. Geochimica 43 (5), 477–488. https://doi.org/10.19700/j.0379-1726.2014.05.006 (in Chinese).
Wu, X., Tao, X., Hu, G., 2014b. Geochemical characteristics and source of natural gases from Southwest depression of the Tarim Basin, NW China. Org. Geochem. 74, 106–115. https://doi.org/10.1016/j.orggeochem.2014.02.002.
Yang, H., Chen, Y., Tian, J., et al., 2020. Great discovery and its significance for ultra-deep oil and gas exploration in Well Luntan-1 of the Tarim Basin. China Petrol. Exp. 25 (2), 62–72. https://doi.org/10.3969/j.issn.1672-7703.2020.02.007 (in Chinese).
Yu, C., Tian, X., Li, J., 2013. The characteristics of light hydrocarbon in oil-associated gas and its application in platform area of Tarim Basin. Nat. Gas Geosci. 24 (5), 774–783 (in Chinese).
Yu, C., Hu, G., Huang, S., et al., 2024. Geochemical characteristics and applications of light hydrocarbons in deep to ultra deep natural gas in China: taking Tarim and Sichuan basins as examples. Nat. Gas Geosci. 35 (5), 917–924. https://doi.org/10.11764/j.issn.1672-1926.2024.04.002 (in Chinese).
Zhang, D., Li, M., Qiao, R., 2025. Applications of light hydrocarbons in petroleum geochemistry: a review. Earth Sci. Rev. 267, 105164. https://doi.org/10.1016/j.earscirev.2025.105164.
Zhang, S., Gao, Z., Li, J., et al., 2012. Identification and distribution of marine hydrocarbon source rocks in the Ordovician and Cambrian of the Tarim Basin. Petrol. Explor. Dev. 39 (3), 285–294. https://doi.org/10.1016/S1876-3804(12)60046-9.
Zhang, S., Su, J., Wang, X., et al., 2022. Sedimentary environments of Cambrian-Ordovician source rocks and ultra-deep petroleum accumulation in the Tarim Basin. Acta Geolog. Sinica-English Ed. 96 (4), 1259–1276. https://doi.org/10.1111/1755-6724.14982.
Zhang, Y., 2008. Genetic Analysis on Es4 nature gases in northern steep slope of Dongying Depression—An example of well Fengshen 1. J. Oil Gas Technol. (J. Jianghan Petroleum Inst.) 2, 394–398. +652 (in Chinese).
Zhou, X., Lü, X., Zhu, G., et al., 2019. Origin and formation of deep and superdeep strata gas from Gucheng-Shunnan block of the Tarim Basin, NW China. J. Petrol. Sci. Eng. 177, 361–373. https://doi.org/10.1016/j.petrol.2019.02.059.
Zhu, G., Zhang, B., Yang, H., et al., 2014a. Secondary alteration to ancient oil reservoirs by late gas filling in the Tazhong area, Tarim Basin. J. Petrol. Sci. Eng. 122, 240–256. https://doi.org/10.1016/j.petrol.2014.07.017.
Zhu, G., Zhang, B., Yang, H., et al., 2014b. Origin of deep strata gas of Tazhong in Tarim Basin, China. Org. Geochem. 74, 85–97. https://doi.org/10.1016/j.orggeochem.2014.03.003.
Zhu, G., Chen, F., Wang, M., et al., 2018. Discovery of the lower Cambrian high-quality source rocks and deep oil and gas exploration potential in the Tarim Basin, China. AAPG Bull. 102 (10), 2123–2151. https://doi.org/10.1306/03141817183.
Zhu, G., Milkov, A., Li, J., et al., 2021. Deepest oil in Asia: characteristics of petroleum system in the Tarim basin, China. J. Petrol. Sci. Eng. 199, 108246. https://doi.org/10.1016/j.petrol.2020.108246.
Zou, C., Wei, G., Xu, C., et al., 2014. Geochemistry of the Sinian–Cambrian gas system in the Sichuan Basin, China. Org. Geochem. 74, 13–21. https://doi.org/10.1016/j.orggeochem.2014.03.004.